Lund University

Master Thesis (60 credits)

Separation of Deformable Hydrogel Particles in the Deterministic Lateral Displacement Devices

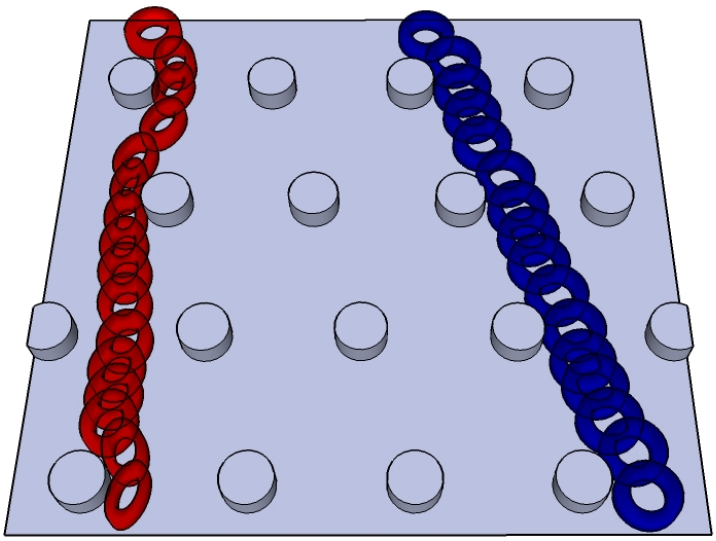

Author:
Masoomeh Ghasemi

Main Supervisor:
Dr. Jonas Tegenfeldt

2012

Separation of Deformable Hydrogel Particles in the Deterministic Lateral Displacement Device

Master Thesis

Author:
Masoomeh Ghasemi

Main Supervisor:
Dr. Jonas Tegenfeldt

Co-supervisors:
Stefan Holm
Dr. Jason Beech

Division of Solid State Physics
Department of Physics

2012

Abstract

In the project, the behaviour of deformable non-spherical microparticles in deterministic lateral displacement (DLD) devices [1] has been investigated. We generated models of biological particles with tunable size, shape and mechanical properties using stop-flow lithography (SFL) [2] to explore how these parameters play a role in our microfluidic separation devices.

The DLD is a microfluidic device and consists of arrays of obstacles which are shifted laterally in each subsequent row. Deterministic trajectories of particles in a DLD array are determined based on their effective size. Thus depending on the orientation of non-spherical particles or the deformation of soft particles, they can show different effective sizes.

In a previous study by Beech *et al.* [3], healthy and disease-modelled red blood cells were sorted in the DLD based on their deformability that verified the capability of the device in deformability-based separation. Also, Holm *et al.* [4] controlled the orientation of the non-spherical particles in the DLD device with various depths resulting in shape-based separation.

Prior to the present study, Mattias Björnmalm, a master student in Nanoscience configured the SFL set-up (summer 2011). A LabView VI was also written by him to control the polymerization process automatically.

To better understand the complex behaviour of deformable particles, we have been looking at a range of deformable polymeric particles with the same size and shape but varying in structure (e.g. solid and hollow structures). We observed different modes of motion for these two types of particle structures at various shear rates. Hollow particles showed a high degree of deformation, while no deformation was observed for solid particles

even at high pressures (high shear rates). At low shear rates in which the deformation of hollow particles was not detectable, they freely rotated as the result of interaction with the posts in the device. The rotation was also observed in the case of solid structured particles.

Different behaviour of these particles resulted in showing up in different trajectories at the exit of the array. Hollow particles showed no noticeable displacement in the device. However, solid particles were laterally displaced as if they are rigid particles.

In future, the detailed analysis of the behaviour of solid and hollow structures is suggested. Also, the deformability of these particles in a shallower device in which the rotation in one dimension is limited can be measured. Moreover, using spherical polymeric particles, a comparison between symmetric and asymmetric shapes can be performed.

Acknowledgments

Firstly, I would like to thank Dr. Jonas Tegenfeldt for giving me the opportunity to work in his research group. You were always concerned and supportive.

Secondly, I give my special thanks to Dr. Jason Beech and Stefan Holm to be such knowledgeable and great co-supervisors. I appreciate all the time you spent on discussions, brainstorming and helping me in the lab.

I appreciate the help that Mattias Björnmalm gave me regarding the stop-flow lithography.

I am grateful to Henrik Persson who helped me with the confocal images.

There are many people in bio-group who has been helpful in many different ways especially Cassandra Niman, Mercy Lard, Farnaz Yadegari, Mehri Baktash and Karl Adolfsson.

Last but not least, I want to thank my dear husband Abbas Saadatnia who is always a great support to me. Thank you with all my love.

List of Acronyms and notations

α	correction factor in calculation of critical size
β	width of the first streamline
$\Delta\lambda$	row shift
η	viscosity
γ	shear stress
λ	center-to-center post distance
ω_0	aspect ratio
ρ	density
τ	shear rate
θ	migration angle
ε	row shift fraction
a, r	radius
D	diffusion coefficient

D_c	critical diameter
f_j	density forces
G	gap size
h	height
k_B	Boltzman constant
L	length
L_0	characteristic length
N	periodicity
p	pressure
Pe	Péclet number
Q	flow rate
R	resistance
R_{eff}	effective radius
Re	Reynolds number
T	temperature
t	time
v	velocity
V_0	characteristic velocity
w	width
x	distance
AFM	atomic force microscopy

CFL	continuous flow lithography
DEP	dielectrophoresis
DLD	deterministic lateral displacement
HFL	hydrodynamic flow lithography
LRL	lock release lithography
PBS	phosphate buffered saline
PEG	polyethylene glycol
RBC	red blood cell
SFIL	stop flow interference lithography
SFL	stop flow lithography
UV	ultraviolet

Contents

Chapter 1

Introduction

Classification of biological and non-biological particles is of paramount importance in various fields of research and industry including biology, medicine, tissue engineering and food industry. The separation parameters are typically the size, the shape and the mechanical properties of particles. Deterministic lateral displacement (DLD) devices introduced in 2004 by Huang *et al.* [1] are capable of sorting based on size, shape [4] and deformability [3]. In DLD devices, deterministic trajectories of particles are determined based on their effective size. This work focuses on deformability-based separation of synthesized polymeric particles as cell-mimics and is a continuation of the recent work by Beech *et al.* [3].

Deformabiliy of cells is an inherent marker because cells reveal different degrees of rigidity depending on their state of health or even during their life cycles. Previously introduced deformability-based microfluidic methods have been shown to accomplishing successful results, however they often suffer from clogging, low throughput and diluted sample requirements. DLD devices offer an alternative where these issues are significantly less of a problem. Furthermore, DLD devices are simple, cheap, have high throughput and offer high resolution for cell separation. In addition, they are also capable of integrating separation based on other driving forces such as dielectrophoresis [5] rather than the normal steric interaction. It is possible

to measure the deformability rate of the deformable particles as a results of the applied shear stress. In addition, this rate can be determined in different dimensions by controlling the orientation of particles in devices of varying depth.

Polymeric particles were chosen because they resemble biological cells in terms of mechanical properties. Also, their size, shape and internal structure are tuneable. We synthesized hydrogel particles through stop-flow lithography (SFL) introduced by the Doyle group [2].

This thesis begins with a short summary of microfluidic theory within the field of DLD devices in **chapter 2**.

Then, in **chapter 3**, the principle of separation in a DLD device is discussed. Also, the details of device design is included.

After that, in **chapter 4**, the SFL technique is explained as well as demonstrating the fluorescent and confocal images of the polymeric particle that we synthesized.

In **chapter 5**, we review the current approaches in deformability-based particle separation with special emphasis on microfluidic-based methods. The advantages and drawbacks of each method are discussed in there.

In **chapter 6**, a description of experiments used to characterize our polymerized particles in a DLD device is shown.

Chapter 7 deals with the results of the experiments and the corresponding plots are included.

In **chapter 8**, a discussion of the experimental results is given. Also, the results of two similar studies about soft particles are discussed.

Finally, the thesis ends with the conclusion in **chapter 9**.

Chapter 2

Microfluidic Theory

Microfluidics is a new field of science and technology that deals with micro-scale amounts of fluid. Recently, numerous microfluidic devices for a variety of applications including cell analysis, mixing, sensors, etc. have been introduced. Thus, prior to dealing with our microfluidic device in the next chapter, we will discuss the physics of microfluidics [6, 7, 8].

2.1 The Reynolds number

The Navier-Stokes equation, for Newtonian fluids, derived from the Newton's second law is written as [9]:

$$\rho[\partial_t v + (v.\nabla)v] = \sum_j f_j \tag{2.1}$$

$$\sum_j f_j = -\nabla p + \eta\nabla^2 v + f \tag{2.2}$$

where the first term to the left of the equation 2.1 describes the inertial acceleration and the right side shows the density forces. Density forces include pressure gradient ($-\nabla p$), viscous force ($\eta\nabla^2 v$) and body forces such as the gravity and steric interactions. The non-linear term of the Navier-Stokes equation ($(v.\nabla)v$)is difficult to solve mathematically. However, this

equation can be simplified in some cases. One approach is to change the Navier-Stokes equation into a dimensionless equation.

In micro-scale lengths, when the viscous term (the term to the right of the equation, excluding body forces) dominates, the non-linear inertial term is negligible and thus the equation becomes linear:

$$-\nabla p + \eta \nabla^2 v = 0 \tag{2.3}$$

The ratio of the inertial to the viscous term is called Reynolds number (Re) and is defined by:

$$Re = \frac{F_{inertial}}{F_{viscous}} = \frac{\rho V_0 L_0}{\eta} \tag{2.4}$$

where V_0 and L_0 are the characteristic length and velocity, ρ and η are the density and the viscosity of the fluid, respectively. Clearly, the viscous drag is dominant at low Reynolds numbers ($Re \ll 1$).

2.2 Laminar flow

A fluid flow is generally characterized by the Reynolds number (Re). At high Re (> 1500), the flow is said to be turbulent. In this regime the flow changes stochastically. In the regime of $Re < 1$, the flow is laminar, where two co-flowing streams do not mix except by diffusion (Fig. 2.1). In narrow micro-channels, containing a viscous flow with a relatively low velocity, the laminar flow condition dominates. For instance, in a microfluidic channel with the characteristic length of 10^{-3} m containing water with the viscosity and the density of 10^{-3} $kg.m^{-1}.s^{-1}$ and 10^{3} $kg.m^{-3}$, respectively; when the velocity of the fluid ranges between $10^{-6} - 10^{-3}$ $m.s^{-1}$ the Re is in the range of $10^{-3} - 1$. The flow is therefore laminar. In figure 2.1, two co-flowing laminae are depicted which are in contact but do not mix.

One significant characteristic of laminar flow is the flow profile. The profile actually depends on the driving force that pushes the fluid through a channel. For instance, an electrokinetically driven flow in a micro-channel has a plug-like velocity profile, whereas a flow driven by a pressure gradient is parabolic due to zero velocity of the fluid at the walls (no-slip boundary condition) and maximum velocity in the center of the channel.

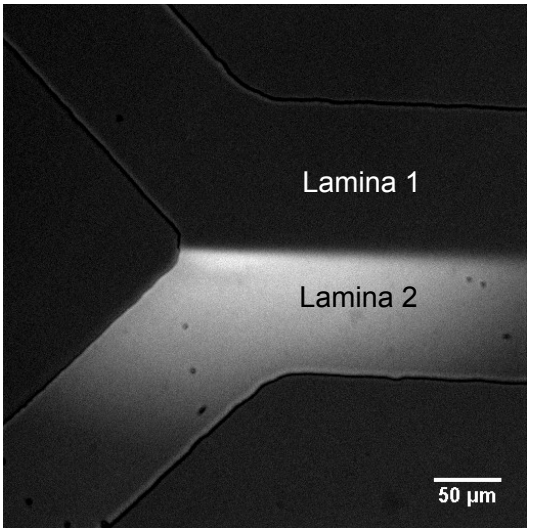

Figure 2.1: Two streams of the same buffer but one containing fluorescent dye in a microfluidic channel meet. However these streams do no mix. Under this condition, the flow is called laminar.

2.3 Diffusion coefficient and Péclet number

At low Re regime, as earlier mentioned, mixing only occurs due to diffusion. The diffusion coefficient (D) of a particle with the radius a in a fluid with viscosity of η is given by:

$$D = \frac{k_B T}{6\pi\eta a} \tag{2.5}$$

where k_B is the Boltzman constant and T the temperature. D is expressed in terms of $m^2 s^{-1}$. For example, the diffusion coefficient of a 20 μm particle in water with the viscosity of 10^{-3} $kg.m^{-1}.s^{-1}$ at room temperature is 2.12 $\mu m^2.s^{-1}$. Defining the mean square distance that a particle diffuse in

one dimension in time t as:

$$< x^2 >= 2Dt \tag{2.6}$$

the particle in the example would diffuse 2 μm in one second. Thus, in length-scales relevant in microfluidics, the diffusion has a significant effect on the resolution of a device, when device function does not rely on it. It must be mentioned that in some cases (e.g. H-filter [10]), this effect is desirable, but in DLD devices, diffusion degrades the resolution. However, by running the device at high flow rates which is possible in DLD devices, this effect is efficiently minimized.

Another important dimensionless number in microfluidics is the Péclet number. It is defined as the ratio of the diffusion to the convection time and written as:

$$Pe = \frac{L_0 V_0}{D} \tag{2.7}$$

Therefore, high Pe number is preferred since it corresponds to high fluid rate and low diffusion coefficient. Last but not least, increasing the flow rate is possible provided that the laminar flow condition remains.

2.4 Particles in the fluid

The dominant force on particles in a fluid at low Re is the viscous drag force. The exerted drag force on a rigid spherical particle of radius r is expressed by:

$$F_{drag} = 6\pi\eta r v \tag{2.8}$$

where η and v are the fluid viscosity and the particle velocity, respectively. Provided that the viscous force is the only force on particles, they will move within the streamlines with the same velocity as the fluid (non-slip boundary conditions). Though, in the presence of other forces other than drag force, particles might cross the streamlines. These forces can be either stochastic like diffusion or deterministic including steric, gravitational, di-electrophoretic forces, etc. In DLD devices, the individual steric hindrance

or a combination of steric and other deterministic forces can be implemented to separate particles. The separation strategy in DLD devices is further discussed in section 3.1.

2.5 Fluidic Resistance

The flow rate (Q) in a micro-channel is dependent on the fluidic resistance of that channel through:

$$Q = \frac{\Delta P}{R} \tag{2.9}$$

where ΔP is the pressure drop across the channel with the fluid resistance R. The resistance of a rectangular channel with the length, height and width of L, h and w can be calculated by:

$$R = \frac{12\eta L}{wh^3}\left[1 - \frac{h}{w}\left(\frac{192}{\pi^5}\sum_{n=1,3,5}^{\infty}\frac{1}{n^5}tanh\left(\frac{n\pi w}{2h}\right)\right)\right]^{-1} \tag{2.10}$$

which can be simplified to:

$$R = \frac{12\eta L}{wh^3} \tag{2.11}$$

for rectangular channels with $w \ll h$ that h denotes the smallest dimension.

The resistance of the channel is a significant parameter that should be considered in designing a DLD device. It is important to be able to define flow rates in the different parts of a device, which for a given pressure depends on the resistance. We will discuss later (section 3.2.2) how we determined what dimensions of the inlet and outlet channels to use in order to fulfil this purpose.

2.6 Shear rate

Particles in a fluid experience a shear stress. This stress is maximum when they pass between two posts where the flow becomes narrow resulting in increasing of the fluid velocity. The shear stress deforms soft particles and

increases with the increasing the pressure. For Newtonian fluids, the shear stress is given by:

$$\tau = \eta\gamma \tag{2.12}$$

where τ and γ are the shear stress and the shear rate, respectively.

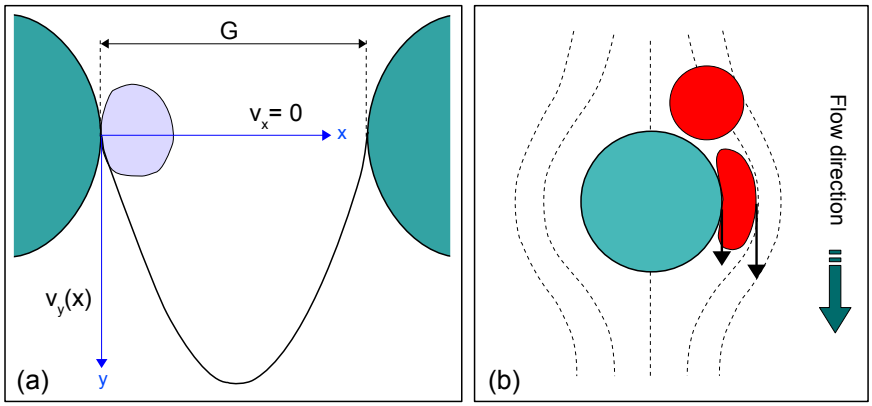

Figure 2.2: (a) The parabolic flow profile between two posts. The velocity is zero in x-direction due to no-slip boundary condition but in y-direction, the velocity is a function of the distance from the wall. (b) A particle feels a smaller velocity near the post, while the velocity on the other side far from the post is larger. This velocity gradient causes a shear rate which deforms a soft particle.

For parabolic flow profiles between two walls, as shown in figure 2.2-a, the velocity in y-direction is calculated by:

$$v_y = \frac{k}{2\eta}(Gx - x^2) \tag{2.13}$$

where k is a constant, G the distance between walls (corresponding to gap width in the DLD device) and x the distance in x-direction. This equation is the solution of equation 2.3, which also gives the zero velocity in x-direction due to no-slip boundary condition. It can be simplified as:

$$v_y = 4v_{max}(\frac{x}{G} - \frac{x^2}{G^2}) \tag{2.14}$$

Therefore, for this simple case with the velocity gradient in one direction, the shear rate is:

$$\gamma = \frac{dv_y}{dx} \tag{2.15}$$

which is expressed in terms of s^{-1}. Clearly, the largest shear rate is at the walls and by substituting 2.14 in equation 2.15 it can be simplified as:

$$\gamma = \frac{4v_{max}}{G} \tag{2.16}$$

For a deformable particle which is travelling with the fluid and passes near a post, it experiences different velocities at its two ends. The side near the post moves slower, but the other side of the particle moves faster. As mentioned, the shear rate is the velocity gradient in y-direction, thus the resulting shear rate deforms the particle as illustrated in figure 2.2-b. The higher the velocity gradient and the shear rate, the larger the deformation.

Chapter 3

Deterministic Lateral Displacement

Deterministic lateral displacement (DLD) is a microfluidic method recently introduced by Huang *et al.* [1] which is used for sorting particles. The device is constructed of an array of micro-posts shifted laterally in each subsequent row. The geometry of posts, the distance between posts and the row shift fraction are determinant parameters in fractionation. The basic idea is that particles smaller and larger than a critical size follow different trajectories as a result of interaction with the posts. The theory of DLD devices is further discussed in section 3.1.

Higher throughput and resolution in separation has been achieved by DLD devices compared to other common size-based sorting methods such as size exclusion [11] and hydrodynamic [12] chromatography. Moreover, deterministic separation in DLD has superior resolving power compared to stochastic fractionation of particles in another microfluidic-based device known as H-filter [10].

In DLD devices, particles have been primarily sorted based on size and recently based on shape by Holm *et al.* [4] and deformability by Beech *et al.* [3]. Blood components were separated from blood plasma in DLD with no dilution by Davis *et al.* [13]. Inglis *et al.* [14] sorted healthy and

malignant lymphocytes based on their size. In another study by the same group [15], they determined the platelet size and morphology in the DLD device. Holm *et al.* [4] demonstrated the fractionation of parasites from blood by controlling particle orientation. In a very recent study, Beech *et al.* [3] considered the deformability of healthy and sick red blood cells as the sorting parameter. Besides biological particles, studies have been carried out in successful separation of suspensions in food [16] and aqueous droplets [17] in the DLD.

Apart from using the characteristics of particles as the sorting parameter, noticeable attention has been paid to the device itself to improve its performance in separation mechanism. Attempts have been made to tune the critical size of an existing device. Beech *et al.* demonstrated the combination of dielectrophoresis (DEP) and DLD resulting in a decrease of the critical size [5]. They also utilized the elasticity of the PDMS-made device to change the critical size during an ongoing separation [18]. In another study, a high flow rate of 115 $\mu L.min^{-1}$ of undiluted blood sample was achieved as a result of integration of six parallel devices [19]. It confirmed high compatibility of DLDs for increasing the throughput. Additionally, modifying the geometry of posts from circular to triangular posts resulted in decreasing the critical size, the pressure requirement and the possibility of clogging [20]. As the final example, Morton *et al.* controlled the trajectories of particles in complex DLD geometries [21].

In this chapter, after a short summary of DLD theory (section 3.1), the details of device design is described in section 3.2. The fabrication procedures are explained in section 3.3. Finally, we describe how to run an experiment with a DLD device in section 3.4.

3.1 DLD Theory

A DLD device consists of arrays of micron-sized posts. These posts are shifted by a fraction of the center-to-center distance between posts in each subsequent row. DLD is illustrated schematically in figure 3.1. Here λ is the center-to-center distance between two subsequent posts and ε is the row

shift fraction:

$$\varepsilon = \frac{\Delta\lambda}{\lambda} \tag{3.1}$$

In this figure, the array repeats itself after three rows; thus, the periodicity of the array is $N = 3$. N is the inverse of the row shift fraction:

$$N = \frac{1}{\varepsilon} \tag{3.2}$$

The gap width (G) is the difference of λ and the post diameter. The row shift can be achieved by tilted square or rhombic arrays. In the present study, the latter was used (Fig. 3.1) in which the rows are perpendicular to the flow direction.

Upon entering the fluid into the gap between two posts and encountering the post in the next row, it is bifurcated into streamlines. The number of streams depends on the periodicity of the array. For instance, in figure 3.1, the fluid is separated into three streamlines, each containing the same amount of fluid flux. Hence, the width of the sub-flows changes because the velocity changes. The stall line is defined as the line beginning from a post in a period and ending on a post in the next one. Stall lines separate the sub-flows in such a way that the index of each streamline decreases by one in each row. Regarding previous example, streamline 3 becomes 2, streamline 2 becomes 1 and so forth.

Now, assume that there are particles in the fluid stream. Particles differing in size would choose different paths in the array. This specific trajectory is decided by the width the first streamline (β) and is equivalent to the critical radius in the device. The critical diameter (D_c) is twice of the critical radius and therefore, twice the width of the first streamline [22]:

$$D_c = 2\beta \tag{3.3}$$

spherical particles smaller in diameter than D_c follow the flow direction and go straight to the bottom of the array. This mode of motion is called "zigzag". On the other hand, when particles diameter is larger than the D_c,

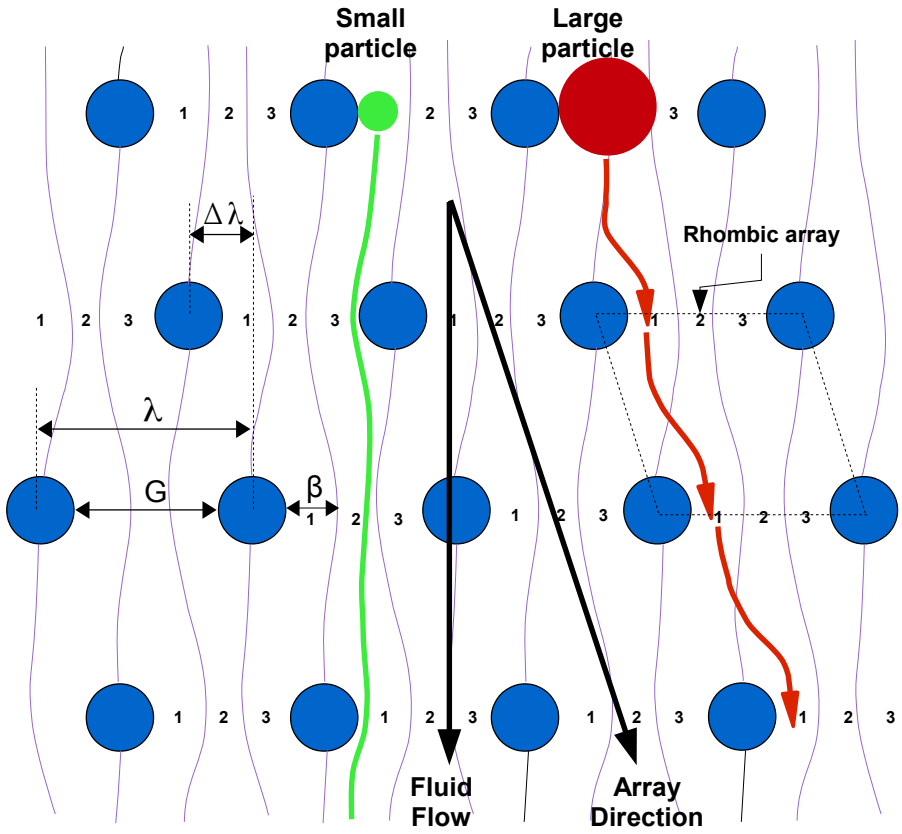

Figure 3.1: The basic principle of the DLD device: particles choose their trajectories based on their size. Particles with smaller diameter than D_c (green particle) travel in the flow direction. But larger particles, $d > D_c$, (red particle) change their streamline and bump to the adjacent one. D_c is twice the width of the first streamline and generally depends on the row shift fraction, ε, and the gap width, G. This array has rhombic unit-cells. This figure is reproduced from the Ref. [13].

they cannot fit in the first flow stream, thus they are forced, by interactions with the post, into the adjacent one. Consequently, they actually move at an angle respective to the flow direction defined by:

$$\theta = arctan(\frac{1}{N}) = arctan(\varepsilon) \tag{3.4}$$

where θ is the migration angle of the device and this mode of motion is known as "displacement". Obviously, increasing the periodicity of the array results in a smaller angle.

To relate the critical size, D_c, to the device characteristics, it can be rewritten as:

$$D_c = 2\alpha G\varepsilon \tag{3.5}$$

The parameter α is involved to account for the parabolic profile of the flow through the gap. For plug-like flow profiles, as in case of electro kinetically driven flow, α is 1, so the width of all streamlines is equal. But, because of no-slip boundary condition near posts (and hence zero velocity) in pressure-driven flows, the width of the first streamline is wider than other streamlines in between. Therefore, α is larger than 1.
All in all, several factors including post shape, post diameter to gap size ratio and the depth of the device affect the critical size [20, 23, 4]. The critical diameter can also be determined empirically as Davis did in [24]. In the present project, this empirical relation was used for critical size measurements:

$$D_c = 1.4G\varepsilon^{0.48} \tag{3.6}$$

Up to now, two modes of motion were introduced which result in separation of different-sized particles. However, this is valid only if the array periodicity, N, is an integer. For non-integer N values, the existence of other modes has been shown [25]. In addition, through 2D simulations, the third mode of motion known as "dispersive" mode is predicted for deformable particles which are larger than half of the gap size [26]. Also, a mixture of zig-zag and displacement motions due to the asymmetry of the flow profile[1] have been observed in a study by Kulrattanarak *et al.* [27].

[1]The asymmetry is due to different widths of the streams between posts.

The last thing to notice here is the non-reversibility of the particle interactions in the flow. In short, as previously mentioned, at the low Reynolds number regime, the dominant force is the time-invariant viscous drag. However, in the presence of diffusion and steric interaction between particles and posts, the fluid flow is irreversible. This results in locking of particles into periodic trajectories which is different from the direction of the driving force. Since the locking direction is predictable for each migration angle, this mechanism can be implemented to enhance the size-based separation in DLD devices [28, 29, 30].

3.1.1 Size, shape and deformability of particles

Particles including biological and non-biological ones differ in shape and mechanical properties. Therefore, except for rigid spherical particles, each particle needs multiple parameters to describe their shape. For instance, in case of a rigid rectangular cubic particle, there is a possibility of showing at least three different size parameters depending on the orientation of the particle in the device. The situation would be more complicated for deformable particles. Nevertheless, for each particle of any shape and deformability, an effective size, R_{eff}, can be defined as the radius of a rigid sphere that travels in the same manner or trajectory as that particle [23]. Figure 3.2 shows how non-spherical and deformable particles can reveal various effective size as a result of their interaction with the posts.

When particles are free to rotate in the device (Fig. 3.2-a), their behaviour is often characterized by their smallest dimension in the interactions with the posts. This consequently influences the effective size. However, it can be used in a controlled way to show a certain dimension of a particle as Holm *et al.* did, and thereby to separate otherwise indistinguishable particles by shape [4].

In the case of separation of deformable and stiff particles (Fig. 3.2-b), the softer particle shows a smaller effective size near the posts respective to the rigid particle with the same shape and dimensions.

Lastly, velocity gradient through the gaps induces shear torques which deform soft particles. Calculating this shear stress is not straightforward

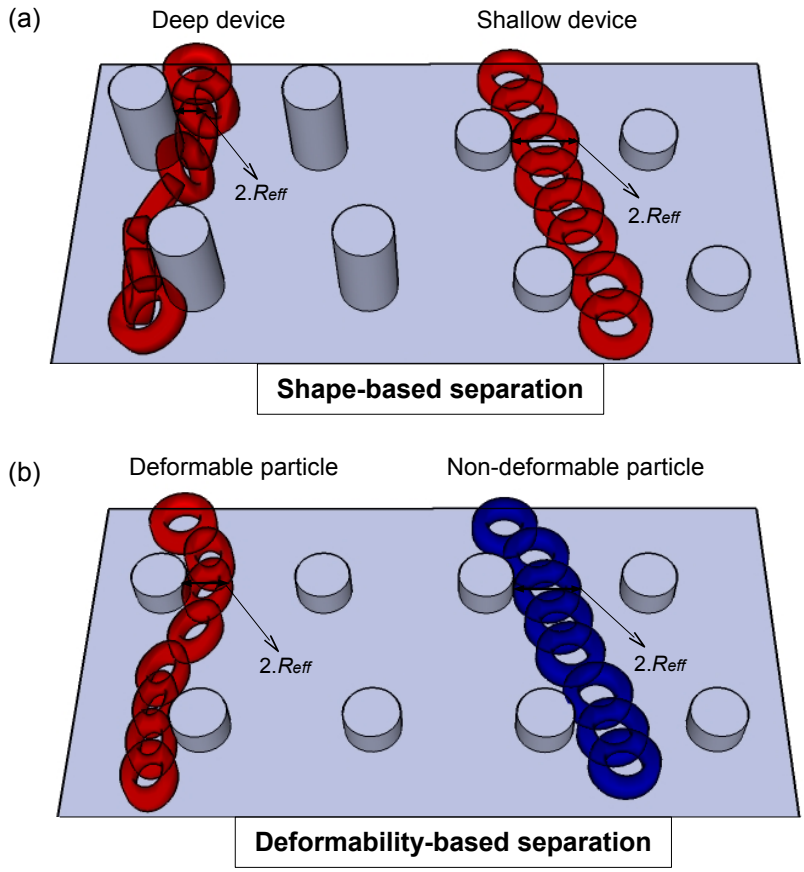

Figure 3.2: (a) Shape-based separation in the DLD device: in a deep device, particles are free to rotate, hence they show their smallest dimensions as they interact with a post. However, in a shallow device, particles cannot rotate freely. Thus, in this example, the particle shows a smaller effective size in the deep device. (b) Deformability-based separation in the DLD device: between two particles with the same shape and size but varying in softness, the more deformable particle (the red one) shows a smaller effective size.

in case of deformable species because both particles and their interactions with posts can disturb the flow. Still, in such situations, R_{eff} of particles can be used [13].

3.2 Device Design

Two DLD devices were designed and fabricated in this project. In this section, the procedure of device design is described. First, we start with the main array of the device, where the separation occurs in section 3.2.1. Next, the design of inlet and outlet channels is explained in section 3.2.2. The last step after calculating size requirements is to design the device layout in L-Edit (Tanner EDA Software Tools) or other vector graphics software. The mask was finally constructed by Delta Mask (Netherlands).

3.2.1 Main array

Depending on separation purposes, the body of the DLD can consist of one array with an individual critical size or several arrays with a range of critical sizes. Single arrays are limited in usage because they only differentiate between two particle populations: particles with smaller and larger effective sizes than the critical size of the array.

On the other hand, multiple separation modes are achieved in a multiple array device, a chirped device or a cascade array. These devices are categorized depending on the parameters that vary in successive arrays (row fraction, gap size or both).

In the present project, the best choice was the chirped array in which the row shift fraction (ε) changes in successive arrays; while, the gap size (G) usually remains constant. To prevent device clogging, G is designed to be more than twice the largest critical size. Separation occurs from the smallest particles at the beginning of the device to the largest ones as the flow goes to the end. Thus, the critical size increases from top through the bottom of the device. However, it is possible to design a reversed chirped array to sort larger particles at the beginning of the device.

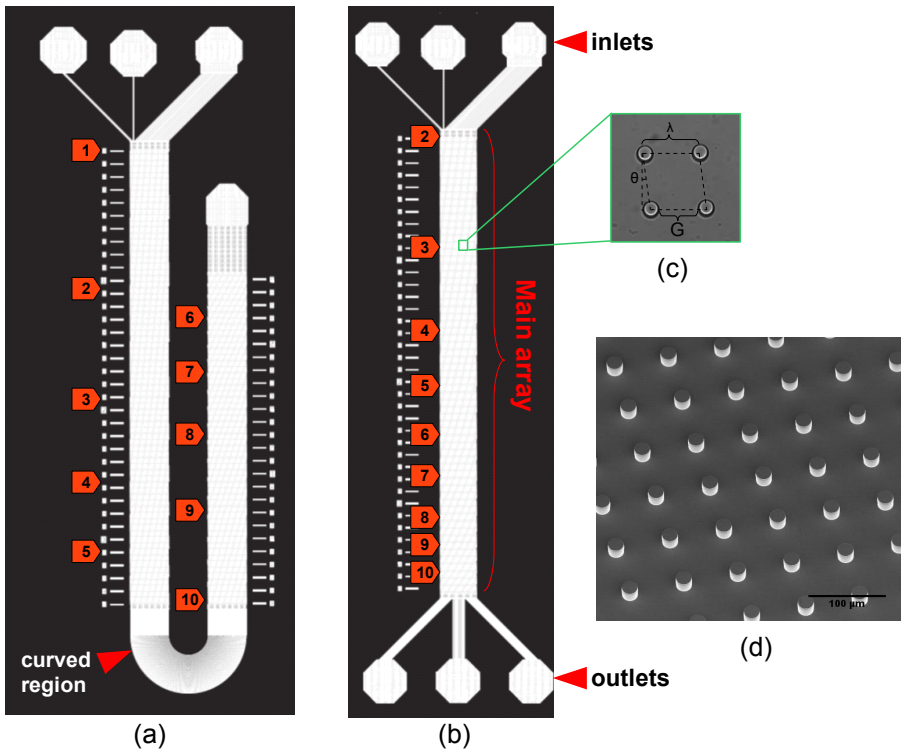

Figure 3.3: The layouts of (a) the curved and (b) the straight DLD devices. Numbers indicate the beginning of each critical region in the main array and start from 2 for the straight DLD layout (to match the numbers in part a), since the critical size starts from 10 μm for that device. There are two periods of each critical section in the straight DLD and section 1 to 5 of the curved device. Sections 6 to 10 in the curved DLD are constituted of 4 period of each array. The curved region connects sections 1-5 of the device to section 6-10. A unit cell of the main array is shown in (c). (d) A SEM image of the array.

Table 3.1: Parameter values for designing of two DLD devices. Practically, for $\Delta\lambda$ varying form 0.2 to 10 μm, periodicities and critical sizes were calculated. Then, integer N-values corresponding to desired D_c were chosen.

Section	Critical diameter $D_c(\mu m)$	Gap $G(\mu m)$	Post diameter (μm)	Row shift $\Delta\lambda(\mu m)$	Period N	Length (μm)	
						Straight	Curved
1	9.0	50	22	1.0	72	-	10368
2	9.8	50	22	1.2	60	8640	8640
3	11.2	50	22	1.6	45	6480	6480
4	12.5	50	22	2.0	36	5184	5184
5	13.7	50	22	2.4	30	4320	4320
6	15.2	50	22	3.0	24	3456	6912
7	16.6	50	22	3.6	20	2880	5760
8	17.5	50	22	4.0	18	2592	5184
9	19.0	50	22	4.8	15	2160	4320
10	21.2	50	22	6.0	12	1728	3456

Figure 3.3 indicates the layouts of two DLD devices, namely curved and straight DLDs. The curved DLD consists of 10 sections with a size of 50 μm and the post diameter of 22 μm. ε varies from 1.2 to 6. There are on the other hand 9 sections in the straight device, with ε varying from 1 to 6; while other parameters are kept unchanged. The critical size varies from 9 μm in the curved DLD (and 9 μm in the straight one) to 21 μm with steps of 1-1.5 μm. This range of critical sizes is chosen to make the device capable of running and sorting particles with 10-20 μm in diameter.

Therefore, particles smaller than 10 μm (or 9μm in the straight DLD) will have no displacement through the device, whereas those particles which are larger than 21 μm in size will bump in all regions down the device. Meanwhile, particles with sizes between 10 μm (or 9 μm) to 21 μm are separated from the smallest to the largest in successive arrays of the device. They are displaced until their diameter is smaller than D_c in that section. At this point, they switch to zigzag mode.

Turning to the critical sizes, they were calculated using equation 3.6;

where $\Delta\lambda$ (Equ. 3.1) varied from 0.2 to 10 at 0.2 μm intervals [2]. Thus, substituting N instead of ε through the relation 3.2, the periodicities were also found. Finally, integer N values were chosen and based on that, the critical sections were defined. Two periods of each array (e.g., two periods of $N = 72$ rows with the D_c of 9 μm) are repeated in the straight device. In the curved DLD, four periods were included for the last five sections (D_c between 15 to 21 μm). A curved section connects the first five sections with two periods of each D_c to the last five sections with four periods (Fig. 3.3). In fact, the reason to design the curved version of the DLD device was the possibility of adding more periods of arrays. This was not achievable in the straight design, because having more than two periods of each array would result in a long device which could not be fitted on the glass substrate of 7 cm length. Of course, enough space for the inlet and outlet reservoirs should be considered. Table 3.1 shows the parameter values for designing both DLD devices.

3.2.1.1 Edge correction

The separation mechanism in pressure-driven DLD arrays works when no discontinuity or boundary disturbs the flow. But the array has a certian width and is constrained to the walls on both sides. Thus, if the gap distances near the side walls are not corrected for this discontinuity in the array, the separation would not be as efficient as in an infinite array [31]. The boundary actually changes the amount of the flow flux which goes to the left upon encountering each post, thus affecting the critical size nearby.

The solution is to correct the first and the last gap widths in such a way to carry the same amount of the fluid to the left of the posts in those gaps as that of posts in an infinite array. Hence, in every array, the first

[2] The smallest size in the device design was limited to 0.2 μm due to limitations in the manufacturing grid during mask processing.

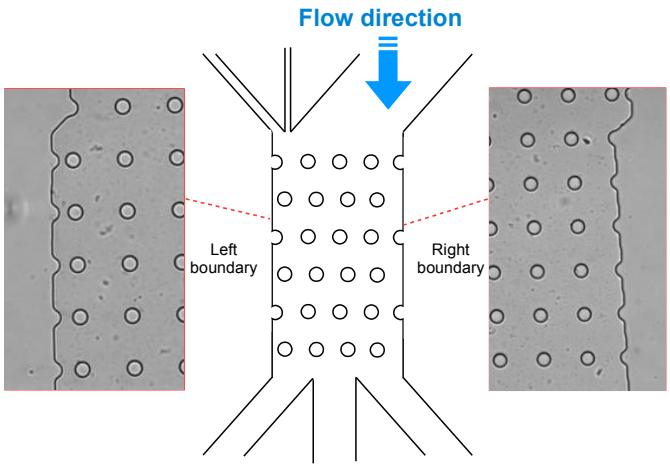

Figure 3.4: The edge correction for both left and right boundaries. For left boundary, the gap width is increasing from the first row of the array and becomes equal to the nominal gap size of 50 μm in the last row. Inversely, on the right boundary, the gap size is decreasing from top to the bottom of the array to reach 50 μm.

and the last gap width is changed in each row according to:

$$g_{n,left} = G\sqrt{\frac{n}{N}} \tag{3.7}$$

$$g_{n,right} = G\sqrt{2 - \frac{n}{N}} \tag{3.8}$$

for the left and the the right boundary, respectively. G is the nominal gap width and n varies from 1 to N. For instance, in the 10th row of the first section, the calculated gap widths are $g_{10,left} = 18.6\ \mu m$ and $g_{10,rigth} = 68.2\ \mu m$. Figure 3.4 shows the edge correction for both side walls.

3.2.2 Inlet and outlet channels

To inject the liquid and to collect the separated fractions, the main array should be connected to inlet and outlet reservoirs. This is done through channels which all have the same fluidic resistance. This ensures entering and flowing parallel streams into the device.

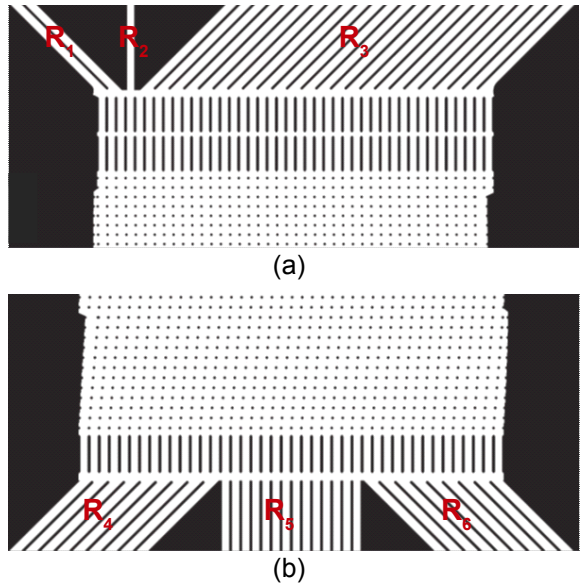

Figure 3.5: (a) The first and the last inlet channels are divided into 2 and 24 channels, respectively, all with the same resistance. R_1 and R_3, in fact, refer to the resistance of narrow channels in the two side inlets. (b) In the case of outlets, the two to the left and right are constituted of 9 narrow channels; while the middle one consists of 14 channels. All these narrow channels have the same resistance.

Usually, there are three inlet channels (Fig. 3.5). The middle one is used for sample injection. The buffer is injected into the other two side inlets and is used to focus and dilute the sample. The width of sample inlet channel depends on the device application. For high throughput purposes, wider channels are preferred while the chirped array with narrow channel

Table 3.2: The dimensions of the inlet channels (channel 1-3) and outlet channels (channel 4-6) are shown in this table. The length and the width of each channel was chosen in a way to give a constant $\frac{L}{w}$ ratio.

Resistance	Channel width (μm)	Channel length (μm)
channel 1	74	7400
channel 2	50	5000
channel 3	74	7400
channel 4	74	7400
channel 5	50	5000
channel 6	74	7400
The fluidic resistance $= 6.10 \times 10^{13} \frac{Ns}{m^5}$		

width is used when throughput is not of importance, as in our case. Thus, the middle channel is 50 μm in width (the same as the gap width).

Side channels are tilted to make room for inlet and outlet reservoir pads. These wider channels on the sides were divided into narrower ones with long posts in between as a support. Wide channels were avoided to prevent collapsing of the device. The total width of the right and left inlets was not equal. However, the width of the outlet channels were chosen to be equal. Six outlet trajectories were included in the straight DLD layout, by dividing each reservoir pad to two separate sections. In the case of curved DLD, only one outlet existed due to the limitation in the final width of the device that should not exceed 2 cm (the width of the glass slide is 2.5 cm).

To have the same fluidic resistance, the ratio of $\frac{L}{w}$ (equation 2.11) was kept constant in all channels. Table 3.2 summarizes the length and width of each channel.

The reservoir pads are large areas (3 $mm \times 3$ mm) with supporting posts. The reservoir tube is glued over these pads after making a hole inside the PDMS slab on this region.

3.3 Fabrication

Using UV lithography, the patterns are transferred to a silicon wafer. Next, the features are replicated on a PDMS layer through soft lithography which is described elsewhere [32]. The master fabrication and soft lithography protocols are included in Appendices A and B, respectively.

In summary, PDMS is mixed with the curing agent in a ratio of 10:1. The mixture is degassed in vacuum and is afterwards poured on the master. Then, the PDMS is cured at 80°C for one hour. The hardened PDMS slab is punched to make holes for fluidic connections. The PDMS layer is bonded to a glass slide using oxygen plasma. Finally, tubes are glued on top of the holes as reservoirs. The whole process is schematically illustrated in figure 3.6.

3.4 Running DLD experiments

Prior to performing an experiment in a DLD device, the surface requires a special treatment to prevent sticking of the sample species to the PDMS or glass surface. The treatment depends on the sample of interest. In our case, the bounded device was treated with an anti-sticking agent (1H,1H,2H,2H-perfluorooctyltrichlorosilnae) in a glove box.

The device turns hydrophobic after surface treatment. When injecting liquid into the device, lots of air bubbles are trapped inside which is difficult to push out of the device. Thus, to run a device, it needs to be degassed. This is done by running the device with the buffer solution for a relatively long time (usually 1-2 hour) to get rid of the air bubbles.

When the device is prepared, it is mounted to an inverted microscope (see figure 3.7). The sample and the buffer are injected into the corresponding inlet reservoirs. Then, the pressure channels are connected from the pressure controller instrument to the reservoir tubes. The pressures at the inlets are adjusted in a way to create a focused stream of the sample flow. Lastly, the recording is performed in the region of interest. In particle tracking experiments, the recordings were taken near the outlets using a

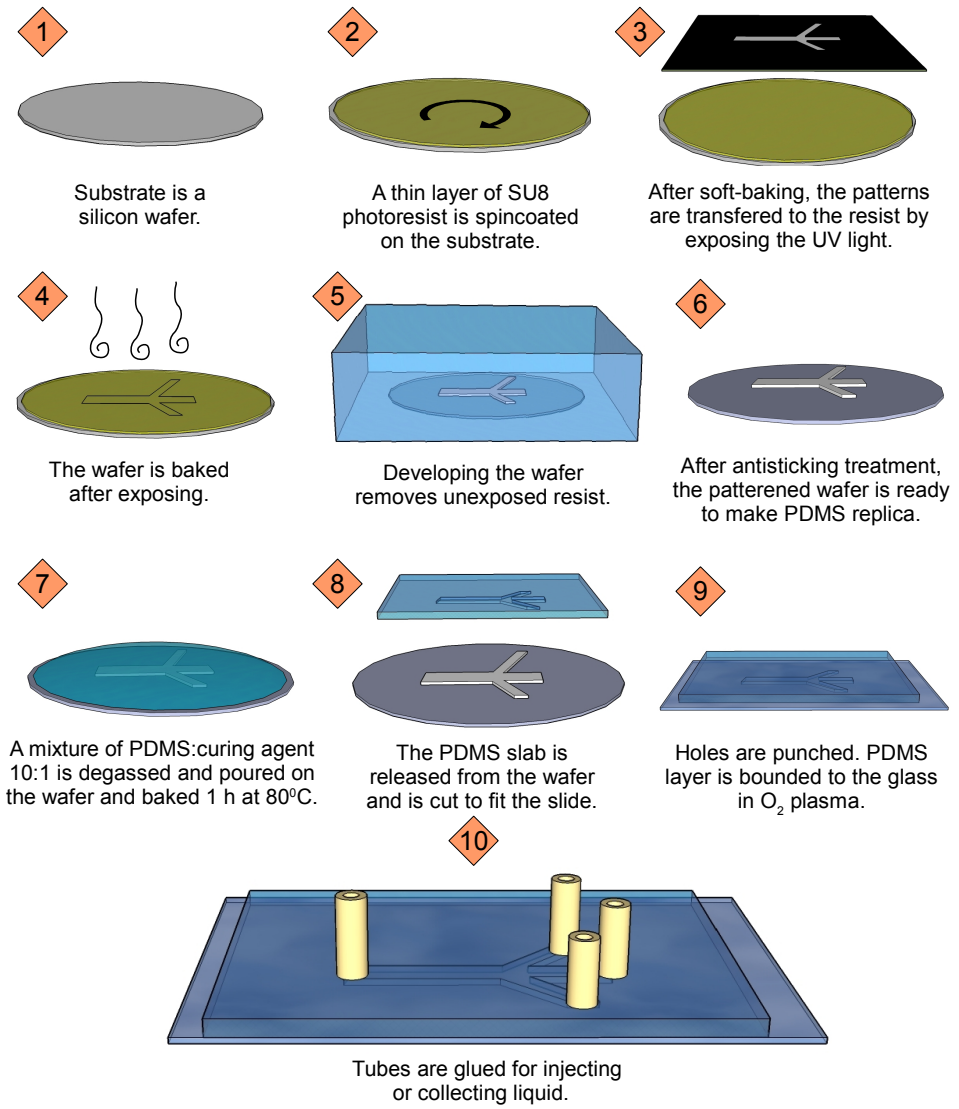

Figure 3.6: The master is made through UV lithography. Steps 1-6 shows how a wafer is patterned with the mask features. After that, the PDMS replica of the master is produced using soft lithography. Steps 7-10 summarize the PDMS microfabrication. This figure is reproduced with permission from Ref. [23].

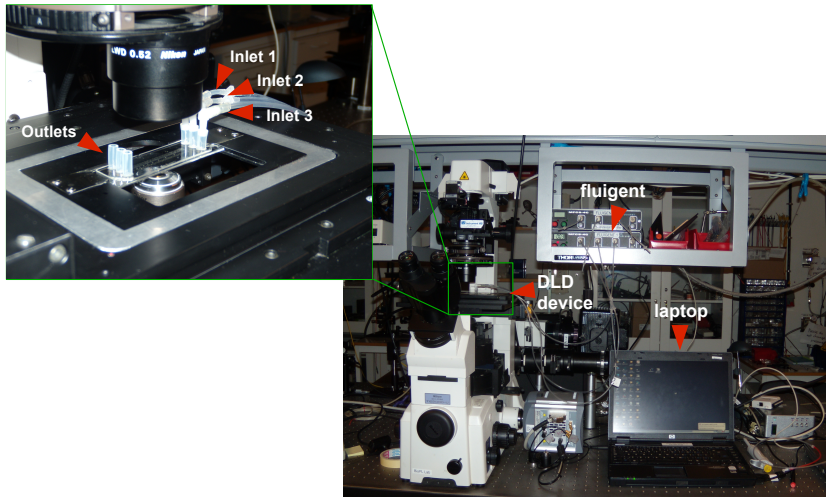

Figure 3.7: The components used when running an experiment with DLD devices: an inverted microscope, a CCD camera, a pressure controller device and its user interface and the DLD device itself. The inset shows the straight DLD device with the inlets connected to pressure channels.

10× objective. But, for observing the deformation of the particles near the posts, the area of interest was a post near the inlet region and the 50× or 60× objectives were used for the recordings. Figure 3.7 indicates the set-up including the components for running an experiment with DLD devices.

Chapter 4

Particle Synthesis through Stop-Flow Lithography

Polymeric microparticles are increasingly used in various areas of research such as photonic [33], biological [34] and clinical [35]. These particles are perfect candidates to be used as cell-mimics, since the monomer precursors can be chosen among biologically compatible materials [36].

The two most common microfluidic approaches for synthesizing hydrogel particles are droplet-based and flow-lithography-based methods. Regarding the former, no mask is required for droplet synthesis, while there are drawbacks. Firstly, droplets are made in two-phase flows (e.g. water droplets in oil). Secondly, only one droplet can be made at a time. Furthermore, the surface of the microfluidic device as well as dispersed and continuous phases need chemical treatment. The most considerable distinction of this method with the particle synthesis through flow-lithography is that the geometry of the droplets are typically spherical or a variation of spherical shapes. On the other hand, the monodispersity of the flow-lithography as well as high control over size, shape, chemistry and the internal structure of the particles are distinct characteristics of this approach [37]. Thus, to fulfil our purpose, we used the latter.

Recently introduced flow-lithography-based methods, mostly by the

Doyle group, including continuous flow lithography (CFL) [38] and stop flow lithography (SFL) [2] are a combination of microfluidics and photolithography. Implementing these methods, the particles are polymerized in a microfluidic channel containing a monomer polyethylene glycol (PEG)-based solution which is illuminated by ultraviolet (UV) light through an inverted microscope. The shape and size of polymeric particles is determined by those of the features on the transparency mask that is projected onto the solution in the channel.

Several variations or modifications of the CFL and SFL have been introduced including lock release lithography (LRL) [39] to produce 3D particles, stop-flow interference lithography (SFIL) [40] to make 3D patterns in the particles through a phase mask and hydrodynamic flow lithography (HFL) [41] to synthesize 3D multifunctional particles. Moreover, the synthesis of multifunctional encoded particles [42] (having more than a million distinct codes), complex particles with controlled curvature [43], chronologically degradable hydrogels [44], cell-laden particles [45] and biological cell-mimics [35] have been reported.

In this project, the stop-flow lithography (SFL) method was used. Contrary to CFL, in which, the particles are polymerized while the flow is continuously moving; in SFL particles are synthesized in "stop-polymerize-flow" cycles. It results in the sharper edge of particles polymerized with SFL as well as an increased throughput and resolution over CFL.

In this chapter, the background theory of SFL will be described first. Then, the details of the experimental part and methods and finally the results will be explained.

4.1 Stop-flow lithography

The requirements for synthesis of microparticles through SFL includes a transparency mask for defining the shape of particles, a microfluidic channel in which the particles are polymerized, the UV light that converts the oligomer solution to polymeric particles, a pressure source and an inverted microscope. A LabView VI is implemented to control the UV light pulses

through the shutter and the pressure pulses. A schematic of these components is illustrated in figure 4.1.

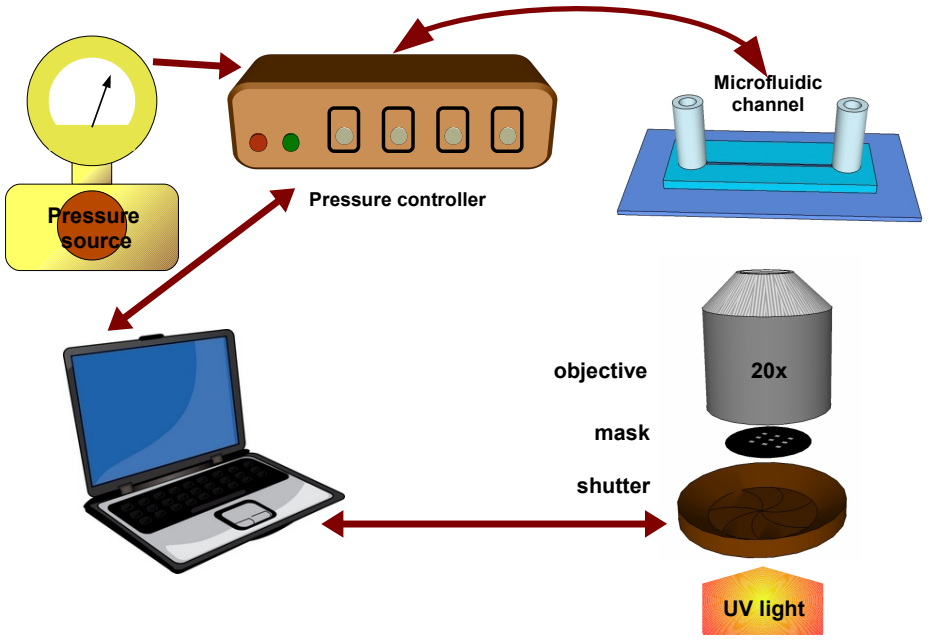

Figure 4.1: Stop-flow lithography: the monomer solution is pushed into a simple microfluidic channel. The flow is stopped and the channel is illuminated by the UV light within a millisecond time scale. The UV light passes through the mask to the channel and the features on the mask are projected into the channel resulting in polymerized particles. The mask feature determines the size and shape of the polymerized particles. Once the particles have polymerized, the flow is started again.

The flowchart in figure 4.2 summarizes a stop-polymerize-flow cycle and shows the shutter and the pressure conditions in each step of a cycle. Also, the snapshots of a real cycle are included in the figure. The oligomer solution stops in the channel (no pressure), the UV light is projected (shutter

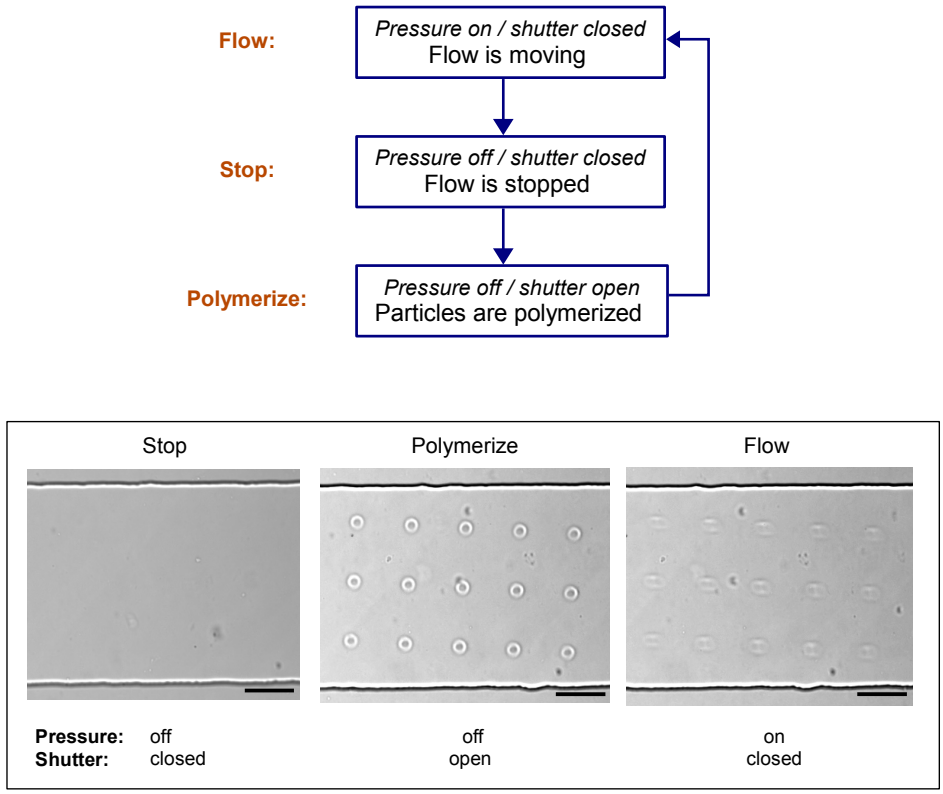

Figure 4.2: The polymerization process is carried out in "stop-polymerize-flow" cycles. A LabView VI controls these cycles. At first, the flow is stopped by applying zero pressure (stop). Next, the UV pulse is projected to polymerize the particles (polymerize). Finally, the pressure is increased from zero to flush out the particles (flow). All scale bars indicate 50 μm.

open) in the channel for a short time (in order of ∼100 ms)creating an array of mask-defined shapes on its way. Particles form based on the features on the mask and are flushed out of the channel to the outlet reservoir by a pressure pulse (shutter closed, pressure open). The solution typically consists of the monomeric PEG and photo-sensitive species. The photo-initiator species reacts with the light photons and creates reactive free radicals. Subsequently, the polymerization of the bond groups of monomer molecules is initiated upon attack by these free radicals [46].

The permeability of the PDMS to gases is an amazing feature which causes this process to happen. In fact, the channel is made of PDMS in both sides. Since oxygen molecules can diffuse in and out of the channel, there is an oxygen layer present in the top and the bottom of the channel. Molecular oxygen reacts with the free radicals (initiator species) and prevents the polymerization [47], thus, hindering polymerized particles from sticking to the PDMS surface. It has been shown that the thickness of this inhibition layer does not depend on the channel height. Typically, it depends on the light intensity, photo-initiator concentration and exposure time. Between these parameters, the increase of of the exposure time is not recommended, because the diffusion time of oxygen would compete with the induction time, thereby preventing polymerization [46]. Therefore, the height of polymeric particles is the difference of the channel height and the oxygen inhibition layer. In our case, the thickness of this layer was about $8 - 10\ \mu m$.

Two important factors determine the required time to expose: the height of the channel and the feature size of the mask [38]. The shallower the channel depth and the smaller the feature size, the longer is the required exposure time. For instance, in our set-up, to synthesize particles with 16 μm in diameter in a channel of 20 μm depth, the required exposure time was between $70 - 110\ ms$.

The SFL technique is capable of polymerizing about 10^7 3 μm-particles per min [2] which is a really high throughput comparing to other methods such as CFL and microfluidic droplet making. In CFL, particles form in a continuous flow. Therefore, to have particles with a sharp edge, the flow should be run at low flow rates. While both SFL and CFL methods

implement the same mechanism for particle synthesis, the possibility of flowing the particles out after formation at high flow rates improves the throughput of the SFL a thousand times respective to the CFL [37].

There is no methodological limitation on the particles size that can be achieved in this approach down to the wavelength of the used UV light ($\sim 400\ nm$). However, the minimum achievable size is practically limited by the minimum printable feature size on the mask as well as the exposure time that cannot be decreased to zero [38]. On the other hand, while the smallest synthesized particle with SFL had a diameter of 1 μm, the interfaces were not as sharp as for larger particles [37]. It has been suggested that, with high quality chromium masks, even down to 400 nm particles can be synthesized through SFL [2].

Finally, when designing the mask, one should take into account the reduction lens in the optical path of the microscope. In our case, there was a 1.67× reduction lens in the optical path. It resulted in a demagnification of 12× of the synthesized particles using the 20× objective respective to the mask ($\frac{20}{1.67} \sim 12$).

In the project, the aim was to synthesize deformable particles ranging from 10 μm to 20 μm in effective diameter differing in shape or aspect ratio using SFL. In practice, a corresponding transparency mask for the 20× objective was used. This means that, a 80 μm length on the mask corresponded to a dimension of 6.7 μm for a particle. The materials and the methodology are described in more details in upcoming sections.

4.2 Experimental

4.2.1 Solution

The monomer solution consists of 65% v/v PEG solution, 15% v/v photo-activator species and 20% DI water as suggested by Haghgooie *et al.* [35]. The PEG solution contains PEG with a molecular weight of 200 u and PEG diacrylate with a molecular weight of 700 u (PEG-DA 700). The particles are labelled by adding 1% of rhodamine B to the solution. This is done by adding 10 mg of rhodamine B in 1 mL of PEG 200 in advance

Softness of the particles is determined by the fraction of the PEG-DA 700. The smaller the PEG-DA 700 fraction, the softer the particles. Since we aimed at synthesizing cell-mimics, the fraction of PEG-DA 700 was chosen as 20% of the PEG solution [1]. This resulted in polymerizing particles with the Young's modulus of $\sim 10\ kPa$ [2] which is close to that of biological cells.

4.2.2 Particle Recovery

The particles were collected after polymerization to be used later in the DLD device. Two methodologies were used for particle recovery. In the first approach [35], we collected particles in a solution containing phosphate buffered saline (PBS) mixed with 0.05% v/v Tween 20 and 40% v/v PEG 200. Afterwards, the solution is spun down for 20 min. The supernatant was taken away and a solution of 0.05% v/v Tween 20 in PBS was added to the sediment.

As an alternative, we directly collected particles in the PBS containing 0.05% Tween 20 and let them to settle down for 1-2 days. This approach was preferred, because it prevented the particles from deforming or ripping out the particles due to the centripetal force. Figure 4.3 shows a population of 13 μm square-shaped cylinders in the outlet reservoir after polymerization.

4.2.3 Microfluidic Device

A simple microfluidic channel with one inlet and one outlet was used for particle synthesis. The channel was 1 cm, 200 μm and 20 μm in length,

[1] The least fraction of PEG-DA 700 that gave reproducible and reliable results with our set-up was 20%.

[2] The Young's modulus of a macro-scale polymerized block was calculated by Mattias Björnmalm during his work on particle polymerization in the summer 2011. He polymerized macro-particles (centimeter-scale blocks) from the PEG solution. Then, the change in the thickness of the particles upon applying a known force across a known area on the top surface of the block was measured. Finally, using the Hook's law, the Young's modulus was calculated.

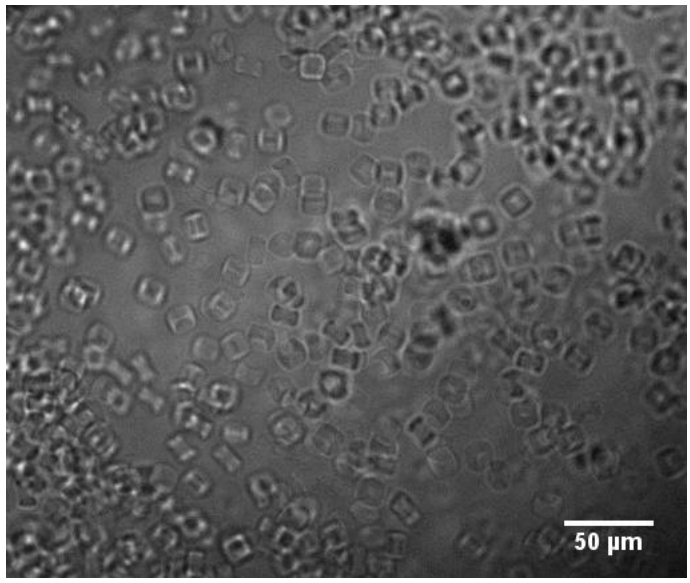

Figure 4.3: An optical microscopy image of the outlet reservoir containing polymerized 13 μm particles.

width and height, respectively. The fabrication process was previously described in section 3.3.
A key requirement is that the microfluidic channel requires surface treatment prior to polymerization. We filled the device with PBS containing 5% Tween 20 overnight. Otherwise, particles stuck to the PDMS or glass surface.

4.3 Hydrogel Particles

This section includes images of polymerized particles. Different shaped particles were all polymerized in the channel with dimensions described in section 4.2.3. The particles ranged in size between $7-16$ μm. A description

of the dimensions of the particles and the corresponding transparency mask follows each figure.

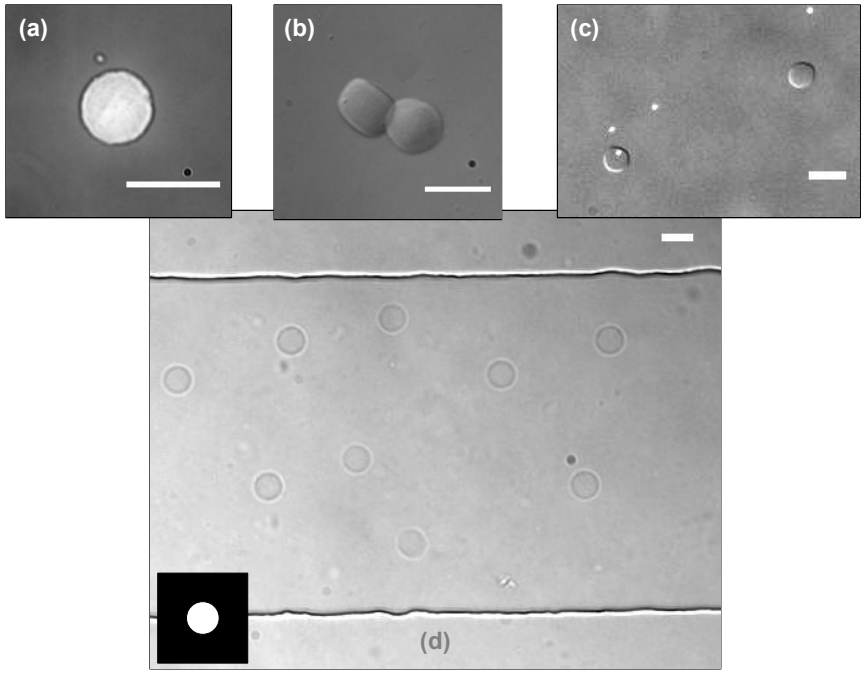

Figure 4.4: Solid cylinders with the diameter of 16 μm and the height of 10 μm. Fluorescence and DIC images of these particles are shown in (a) and (b), respectively. (c) A 3 μm polystyrene bead is encapsulated in one of the two particles. The fluorescent beads can be tracked to analyse the rotation of the particles in the DLD device. (d) Solid cylinders right after polymerization in the microfluidic channel with 200 μm in width. The inset indicates the mask feature for polymerizing these particles. All scale bars are 20 μm.

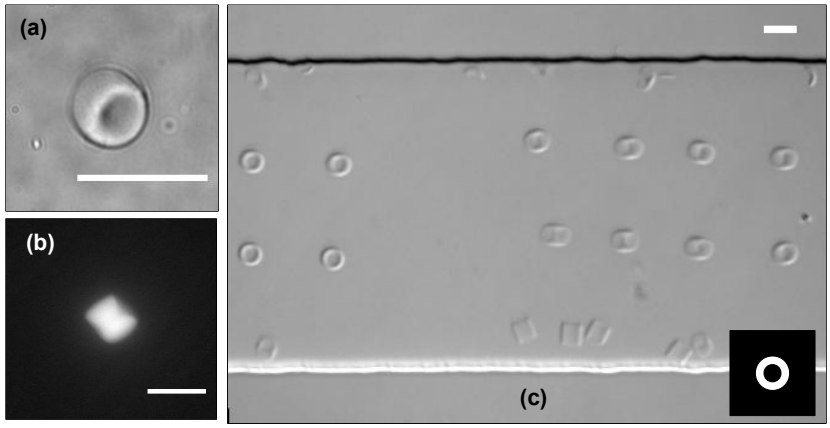

Figure 4.5: (a,b) Fluorescence images of the hollow cylinders with the outer diameter of 13 μm and the height of 12 μm. (c) The DIC image of the hollow cylinders right after polymerization in the microfluidic channel with 200 μm in width. The inset indicates the mask feature for polymerizing these particles. All scale bars are 20 μm.

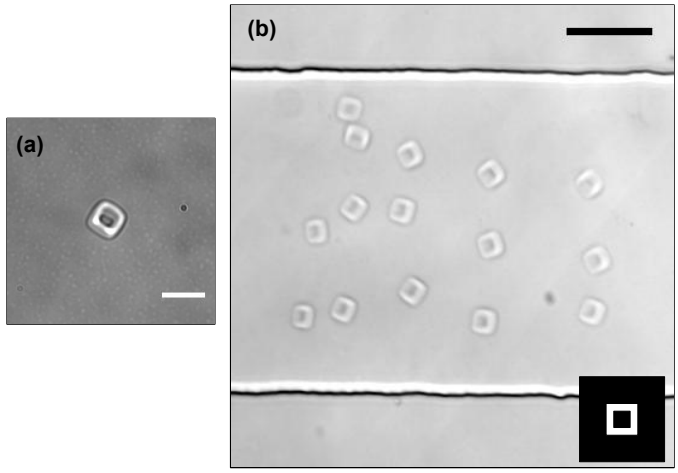

Figure 4.6: (a) Fluorescence image of the hollow square-shaped cylinders with the outer diameter of 13 μm and the height of 10 μm. (b) The DIC image of the hollow square-shaped cylinders right after polymerization in the microfluidic channel with 200 μm in width. The inset indicates the mask feature for polymerizing these particles. Scale bars are 20 μm

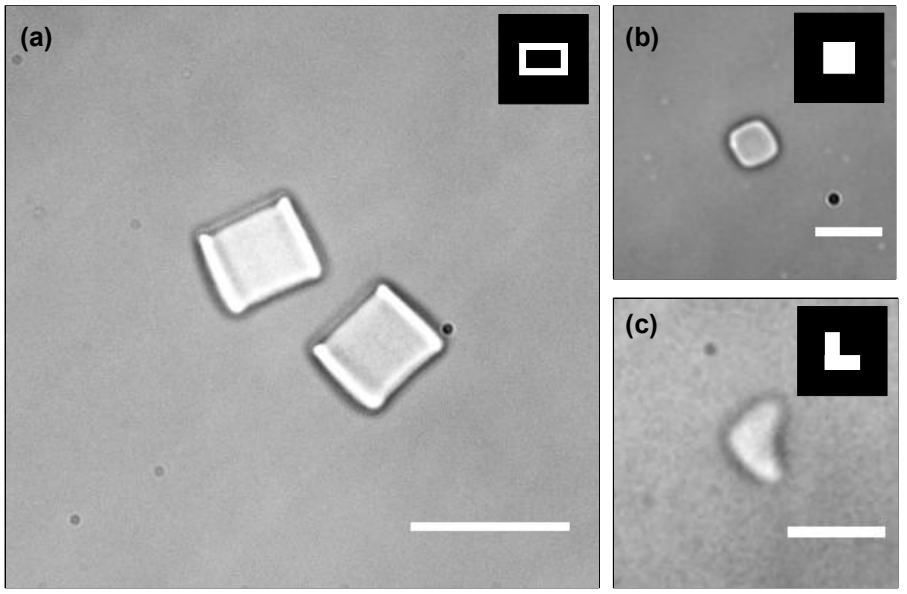

Figure 4.7: Fluorescence images of (a) hollow rectangular-shaped cylinders the outer dimensions of 13 $\mu m \times 6.5$ μm and the height of 10 μm, (b) a solid square-shaped cylinder with the dimensions of 13 $\mu m \times 13$ μm and the height of 10 μm and (c) an L-shaped hydrogel particle with the dimensions of 13 $\mu m \times 13$ μm and the height of 10 μm. For each part, the inset shows the corresponding mask feature. All scale bars are 20 μm.

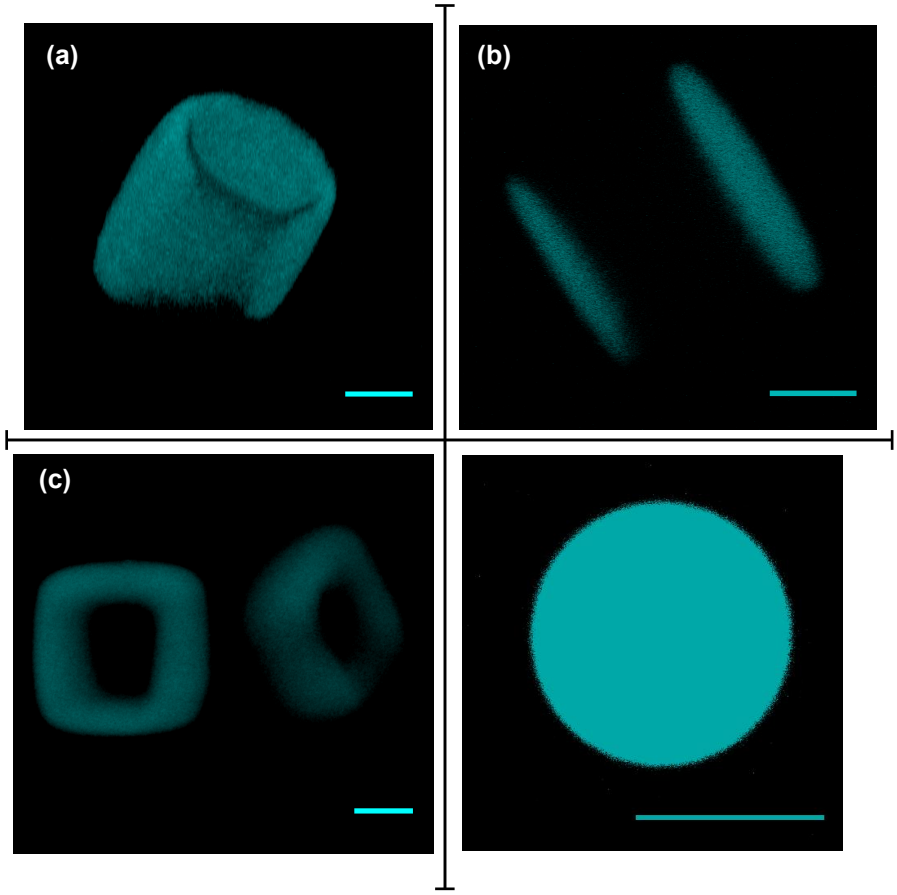

Figure 4.8: Confocal images of a hollow circle-shaped cylinder with the outer diameter of 13 μm (a,b), a hollow square-shaped cylinder with the outer dimensions of 13 $\mu m \times 13$ μm (c) and a polystyrene bead with the diameter of 7 μm. The image of the hollow circle-shaped cylinder in part (a) shows that the bottom of the particle is not polymerized very well. The reason is the non-uniform illumination of the UV light. In such cases, the UV light needs to be aligned. The intersection image of this particle is shown in part (b). To compare deformable hydrogels with a rigid particle, the confocal image of a polystyrene bead was also taken which is shown in part (d). All scale bars show 5 μm.

Chapter 5

Separation Based on Deformability

In general, cells reveal various degrees of deformability depending on their state of health. For instance, due to cancer, a healthy cell with a rigid cytoskeletal network changes to a malignant cancerous cell with a more deformable cytoskeleton [48]. Such alteration of the mechanical properties of a cell is a useful clinical marker in diagnostics.

A number of techniques have recently emerged and shown promise in analysing the deformation of either single cells or cell populations. The very first approaches include micropipette aspiration [49] and atomic force microscopy (AFM) [50]. In the former, a cell is sucked up by a micropipette applying a known suction pressure. The resulting deformability is then measured by measuring the aspiration length. However, in spite of the widespread usage and also the recent optimization of this technique [51], it still probes one single cell at a time. Regarding the AFM technique, not only suffering from low throughput, other factors such as special sample preparation as well as complexity and costly operation system makes it an unsuitable method to be used in various clinical situations.

Along with the advent of microfluidics which eases the delivery of cells and the fabrication of narrow capillaries analogous to those in a living or-

ganism, several microfluidic-based methods for analysing and separating based on the mechanical properties of cells were introduced. These include the laser stretcher [52, 53], microfluidic flow cytometer [54], cell margination [55], inertial focusing [56] and deterministic ratchets [57, 58]. Moreover, the separation based on particle deformability in the deterministic lateral displacement device was recently studied [3]. It is also worth mentioning that, based on simulations, a number of theoretical studies on the design of such microfluidic devices [59, 60] or the analysis of particle behaviour in an existing device [26] have been carried out. Figure 5.1 summarizes the basic principle of the microfluidic devices mentioned above, which are used to classify cells or synthesized particles based on their deformation.

In laser stretcher (Fig. 5.1-a) two counter-propagating laser beams trap a single cell moving along the laser beam. The cell is therefore stretched due to the induced surface forces. The precision of the optical deformability is such that it is possible to distinguish between metastatic and non-metastatic cancerous cells, making it a robust technique for early diagnosis of the disease. Combining microfluidic delivery with the laser stretcher, this method is capable of high speed analysis of individual cells. However, the artificially induced field force might be different from that a cell experiences in a living organism.

The second approach (Fig. 5.1-b) utilizes the same mechanism as micropipette aspiration, but instead simulates a human's capillary as a micropore known as "deformability cytometer". Upon entering cells into the pores, the deformability measurements are performed. This method was tested in the case of malaria infected cells. The disease degrades the deformability of RBCs as it progresses. Thus, late-stage infected cells are the least deformable cells and cannot enter the capillary. Whereas, the possibility of finding ring-stage parasite infected RBCs (intermediate state of the cells in the disease) in the blood, which are more deformable than the late-stage ones, is higher in orders of magnitude. They can therefore be targeted for diagnostic purposes. The drawback of this technique on the other hand is the high risk of device clogging due to narrow entrances.

Another interesting technique to separate less deformable malaria infected cells from healthy rigid cells is "cell margination" (Fig. 5.1-c). The

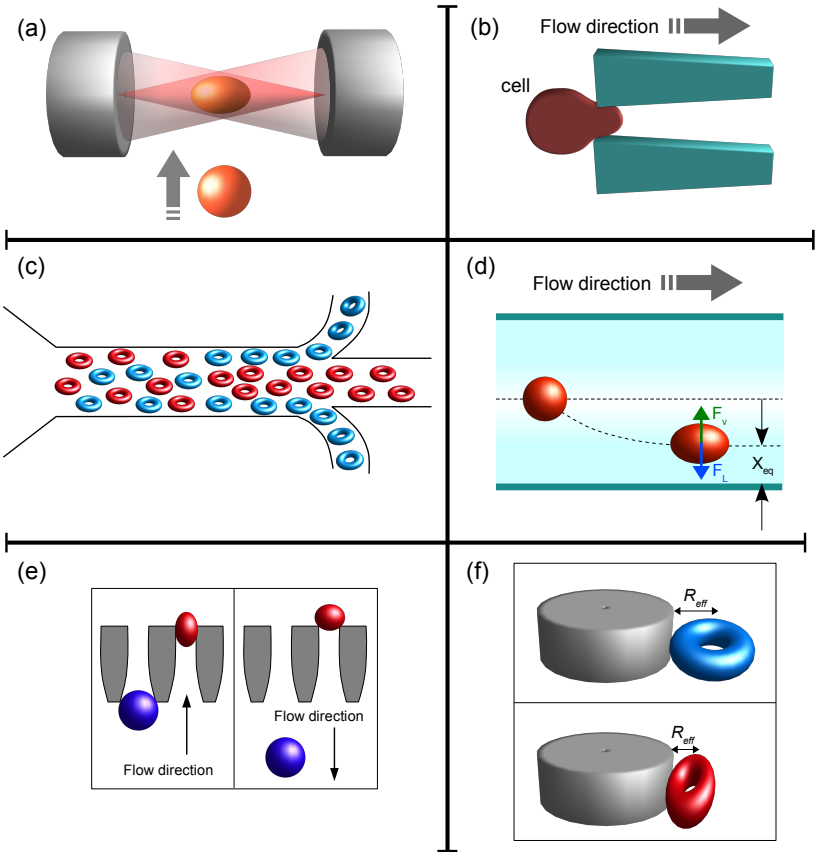

Figure 5.1: (a) Laser stretcher: particles are trapped and deformed by two counterpropagating laser beams[a]. (b) Deformability cytometer: deformable particles are squeezed into narrow constrictions[b]. (c) Cell margination: due to inertial forces, stiffer particles are displaced to the sidewalls, while deformable particles move in the center[c]. (d) Inertial focusing: the lateral position (X_{eq}) of particles is determined as a result of a balance between inertial (F_L) and viscoelasticity (F_v) forces[d]. (e) Microfluidic ratchet: the flow is oscillatory between funnels of different lengths at two ends[e]. (f) DLD: for two particles with the same diameter (red and blue), the rigid one shows larger effective size (R_{eff}).

[a] see [53] Adapted from Biophysical Journal, 88/4, Guck et al., Optical Deformability as an Inherent Cell Marker for Testing Malignant Transformation and Metastatic Competence, Page 3690., Copyright (2005), with permission from Elsevier.

[b] see [54] Reproduced by permission of The Royal Society of Chemistry. http://dx.doi.org/10.1039/c01c00472c

[c] see [55] Reproduced by permission of The Royal Society of Chemistry. http://dx.doi.org/10.1039/c003873c

[d] see [56] Reproduced by permission of The Royal Society of Chemistry. http://dx.doi.org/10.1039/c01c00595a

[e] see [58] Reproduced by permission of The Royal Society of Chemistry. http://dx.doi.org/10.1039/c21c21045b

idea is that the stiffer cells go to the sidewalls, while the pressure gradient force pushes the deformable RBCs to travel in the center similar to what happens in a real capillary where larger and stiffer leukocytes undergo margination. After successful classification of malaria infected and uninfected cells, the process was repeated in the presence of leukocytes. As expected, both leukocytes and infected RBCs were collected in the side outlets. Though the device requires further optimization to separate leukocytes and sick cells in different outlets or even cell populations with various deformabilities.

Another continuous and label-free technique capable of sorting cells based on size and deformability is inertial focusing (Fig. 5.1-d). In this device, the balance between the inertial lift force and the viscoelasticity induced force results in the lateral focusing of the particle stream and the separation of deformable particles from rigid ones. However, a highly diluted sample should be used in the device to prevent the defocusing of particles due to their interactions with one another.

The idea of microfluidic deformability-based ratchets [57] was implemented in the design and fabrication of a device consisting of funnel constrictions [58] (Fig. 5.1-e). The flow moves in an oscillatory fashion in this device. In the forward direction, smaller and deformable cells (shown in red) are squeezed through the funnel. Larger and stiffer particles (shown in blue) on the other hand are excluded since the distance between funnels is smaller than the diameter of these particles. To avoid clogging, the flow direction is then reversed. Now smaller particles cannot pass back into the funnel due to the narrower entrance in this direction. While this approach seems promising for classification of a low-concentrated cell population, the ideal operation is achieved by the manipulation of several micro-valves to provide a uniform flow profile. This results in a rather complicated device design. Moreover, undiluted samples increase the risk of clogging.

Turning to our microfluidic device, DLD, it is possible to sort particles in a heterogeneous population based on their deformabilities (Fig. 5.1-f). The operation principle of the DLD is described in section 3.1. The prominent features of the device are the high throughput and high resolution, low clogging risk, simple and inexpensive design and last but not least the

capability of sorting based on size, shape and deformability simultaneously. Quit recently, Beech *et al.* [3] showed the successful separation of normal, deformable RBCs from less deformable disease-modelled RBCs in DLD devices. The authors also showed that by controlling the particle orientation in devices varying in depth, the deformation of particles in different dimensions can be explored.

Since the behaviour of deformable particles in the DLD device is not fully investigated, this project aimed at analysing this mechanism. However, instead of biological cells, as previously mentioned (chapter 4), synthesized hydrogels are used. This enables us to control the size, shape and mechanical properties of the particles.

Chapter 6

Experiments

The experimental part of the project presented herein is divided into two parts. The first part covers the synthesis and the recovery of hydrogel particles which was dealt with in chapter 4. The second and the main part deals with running these particles in the DLD device, to fulfil two purposes. Firstly, the deformation of particles near the posts was of interest which is described in section 6.1. Secondly, the displacement of the particles varying in size or shape was investigated in the area near the outlet region which is further discussed in section 6.2.

6.1 Hydrogel Deformation

To observe the deformability of particles upon encountering a post in different pressure gradients, the particle stream in the middle inlet was first focused (Fig. 6.1). Afterwards, using a high magnification objective (50× or 50×), the recordings were taken of a region near a post along the particle steam in the standard bright-field or fluorescent microscopy mode. Despite the fact that the particles were fluorescent, it was not possible to record in the fluorescence mode with the available high speed camera (MotionBLITZ), because it was not enough sensitive. On the other hand, with the high speed camera, we were able to record at high frame rates up to

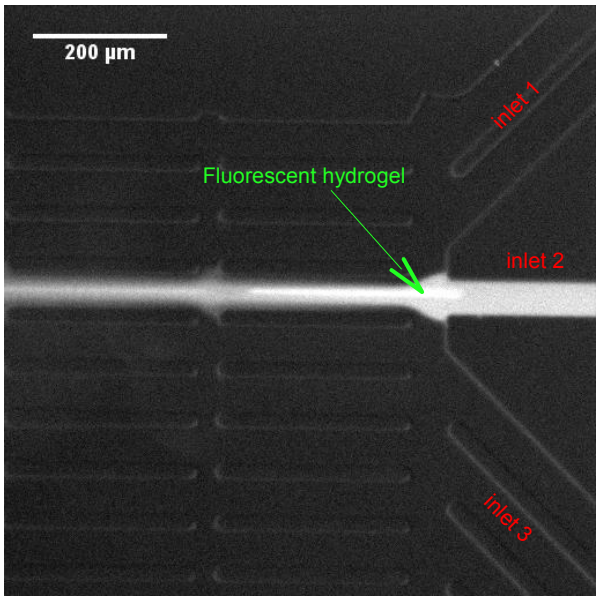

Figure 6.1: The sample flow stream is focused by adjusting the pressures of both side inlets. The green arrow points towards one of the particles in the stream. The white color of the sample stream is due to the leftover fluorescent solution dyes in the sample solution after particle recovery. Also, the particle in the stream which is pointed by the arrow, looks extended because of the long exposure time.

6000 frames per second. Only in the case of hollow circle-shaped cylinders (Fig. 8.1), recordings were performed with a high sensitive CCD camera (Andor Technology) but with a relatively low frame rate of 30 frames per second, at low pressure difference (6.2 $mbar$) in which the velocity of particles was low. The recording was repeated by increasing the applied pressure to find the minimum pressure difference required to deform a particle, as well as determining the deformability rate against the pressure difference.

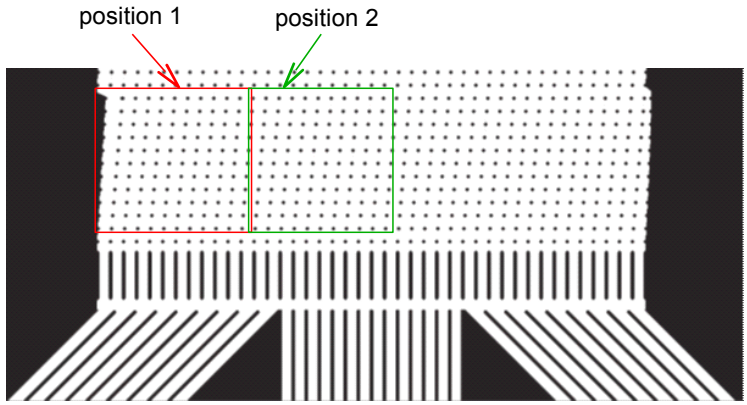

Figure 6.2: The area of interest for particle tracking experiments was the region near the outlets. The recordings were performed with a 10× objective. To fit the field of view with this objective, the area was divided into two overlapping sections which covered gap number 1-22.

6.2 Outlet distribution

After preparing the DLD device as described in section 3.4, the camera was focused on a region near the outlets (Fig. 6.2). In this case, we could not track the particles with the high speed camera because of the poor contrast. Thus, the recordings were performed with the high sensitive camera in fluorescence mode. Since the frame rate we used was around 20 frames per second and we had to count particles using these recordings, this region was divided into two overlapping sections to enable us to use a 10× objective. These two sections covered gaps 1-22; the area where the 16 μm particle would show up. Because the diameter of the particles for these experiments was 16 μm, they could at most be displaced 14 gaps (2× number of critical sections required to change their mode of motion to zig-zag) starting from gap number zero which corresponds to the gap that the background shows up in. Therefore, the most rigid particle would exit from gap number 19. The entrance position corresponds to the fifth gap, thus the maximum

displacement occurs near gap number $5 + 14 = 19$. These two sections are highlighted in red and green in the figure 6.2.

In these experiments, hollow and solid circle-shaped cylinders with a diameter of 16 μm were used. The movies of these two regions were acquired with the same frame rate and with the same duration (1000 frames with the average frame rate of 20 fps). As in the case of the first part, the pressure was increased in $50 - 100$ $mbar$ intervals for high pressure experiments and $\backsim 10$ $mbar$ intervals for low pressure experiments and a new set of data was recorded. The process was then repeated for different types of particles but in a new DLD device.

It is worth mentioning that we only used the straight DLD device. A defect on the silicon master where the curved DLD was patterned made this part of the master unusable. However, this can be easily solved by fabricating a new master when more time is available in future experiments.

Chapter 7

Results

In this chapter, the results of the experiments are reported. First, we demonstrate how differently particles behave near the posts (both their rotation and deformation) in section 7.1. Next, the outlet distribution of 16 μm solid and hollow cylinders is discussed in section 7.2.

7.1 Rotation and Deformation

Once the applied pressure difference was sufficiently low (less than the pressure required to detect the deformation of the particles or when it was not enough to cause a large deformation) particles had freedom to rotate along their journey as a result of interactions with the posts. One example is indicated in figure 7.1. The hydrogel particle is a rectangular-shaped hollow cylinder with the outer dimensions of 6.5 $\mu m \times 13$ μm and the height of 10 μm. The DLD device was an existing device, with the gap width of 25 μm and the depth of 26 μm. The pressure difference in this case was 20 $mbar$. It corresponds to the average velocity of 0.73 $mm.s^{-1}$ and the shear rate calculated from equation 2.16 is 1.2×10^2 s^{-1}. Clearly, the particle changes its direction and thus rotates when it encounters a post.

Increasing the applied pressure gradient increases the shear stress on

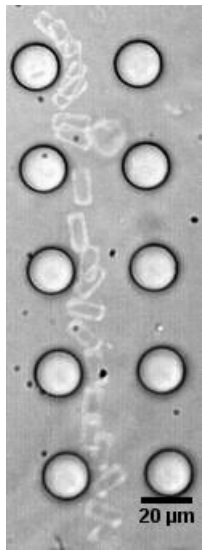

Figure 7.1: The hollow rectangular-shaped cylinder rotates once it meets a post. The outer dimensions of these particles is 6.5 $\mu m \times 13$ μm with the height of 10 μm. The applied pressure is 20 $mbar$ in which the deformation is not detectable.

the particles. What we observed is that the shear forces does not deform our differently shaped hydrogel particles in the same manner. To put it in another words, at the same pressure difference, hollow cylinders showed higher degree of deformation, while no deformation was observed for solid particles. This behaviour is compared in the case of hollow square-shaped cylinders (13 $\mu m \times 13$ μm) and solid circle-shaped cylinders in the figure 7.2.

Hollow square-shaped cylinders (Fig. 7.2-a) are deforming at the average velocity of 4.8 $mm.s^{-1}$ (corresponding to the shear rate of 3.8×10^2 s^{-1}) while making a 90° rotation near the posts. The situation is reversed for solid cylinders (Fig. 7.2-d,e). Even though the shear rate is higher in these cases (7.8×10^2 and 8.8×10^2 s^{-1} corresponding to 9.8 and 11 $mm.s^{-1}$, respectively), they demonstrated no deformation, while red arrows show that the particles have been rotated about 180°. This different behaviour

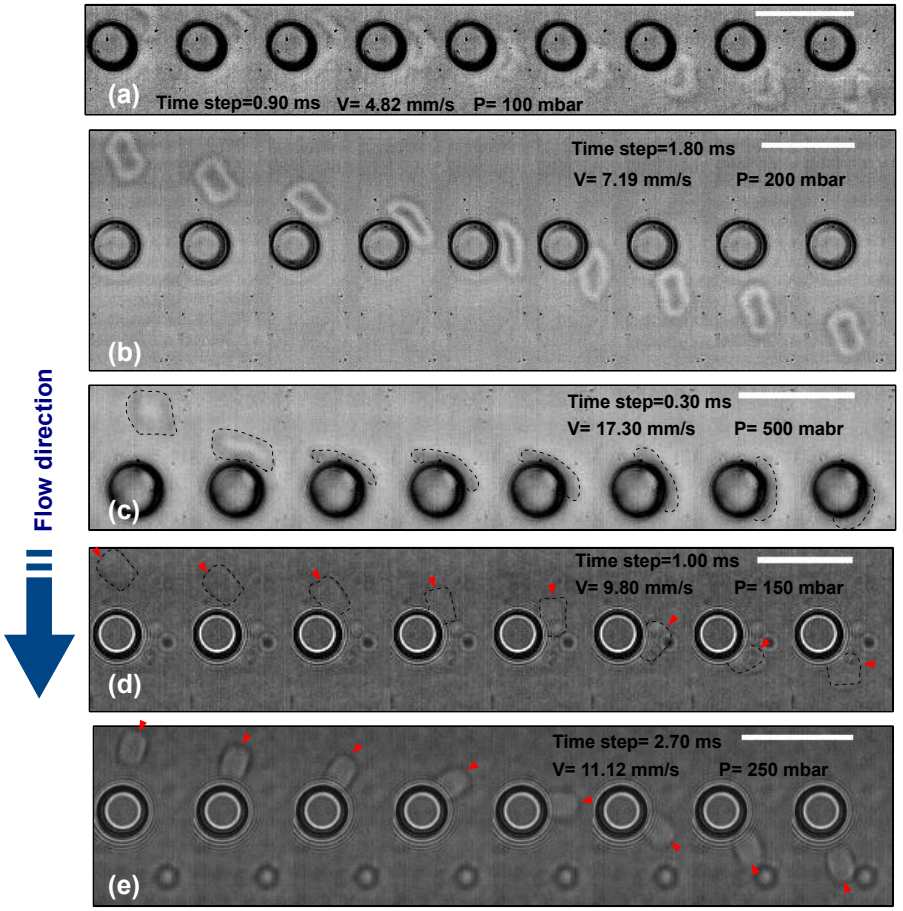

Figure 7.2: The deformation of the hollow square-shaped cylinders (13 $\mu m \times$ 13 μm) at (a) 100, (b) 200 and (c) 500 $mbar$. The effective size is smaller than the unperturbed size of the particle. When the applied pressure is increased the particles show even smaller effective sizes and greater deformation. Solid circle-shaped cylinders (from the side) with the diameter of 13 μm shows no deformation at (d) 150 and (e) 250 $mbar$ but rotates considerably. The recording for the solid circle-shaped particles were done at the same pressures as that of hollow square-shaped particles, but due to the poor contrast, the image of that particle at 500 $mbar$ is not included. The particles in part c and d are encompassed by dashed lines to be distinguished easier. The scale bars indicate 50 μm.

will be discussed later in next chapter. Note that these cylinder-shaped particles in this figure are seen from the side face (with a rectangular cross-section) not from the top (with a circular cross-section). This difference in the behaviour will be later verified (section 7.2) by the outlet distribution of these two different particles.

On the other hand, as indicated in the figure 7.2-b and c, hollow square-shaped cylinders showed even higher deformation with the increased shear rate of $5.7 \times 10^2\ s^{-1}$ and $1.4 \times 10^3\ s^{-1}$, respectively. In spite of the low resolution of the image in part c, it can be distinguished that upon interaction with the posts, these particles have been stretched more at a higher pressure (higher shear rate) comparing to that one at 100 $mbar$, resulting in smaller effective sizes.

It is necessary to declare that this part of the experiments were challenging. Because of nearly the same refractive index of hydrogels and the carrying fluid, we were not easily able to track the particles near the posts with a high speed camera. The situation was even worse with solid particles. Therefore, looking for a way to modify the refractive index of the polymeric particles should be considered for the future experiments.

7.2 Displacement of Hydrogels in the DLD

In this section, the results of analysing the trajectories of particles in the device in two regimes of high and low pressure are included. In the case of high pressure regime, the lateral displacement of 16 μm hollow and solid circle-shaped cylinders through the DLD array are plotted in figure 7.3-a and b, respectively. Also, the corresponding fluorescent images of both position 1 and 2 (see section 6.2, figure 6.2) acquired by overlaying 1000 frames are shown above each plot. These fluorescent images are taken from the recordings at the lowest applied pressure difference (43 $mbar$ and 41 $mbar$ for solid and hollow cylinders, respectively). The number of particles exiting through each gap was counted at each pressure. Then the normalized count number (achieved by dividing the number of particles exiting at each gap to the number of all particles counted in the corresponding pressure)

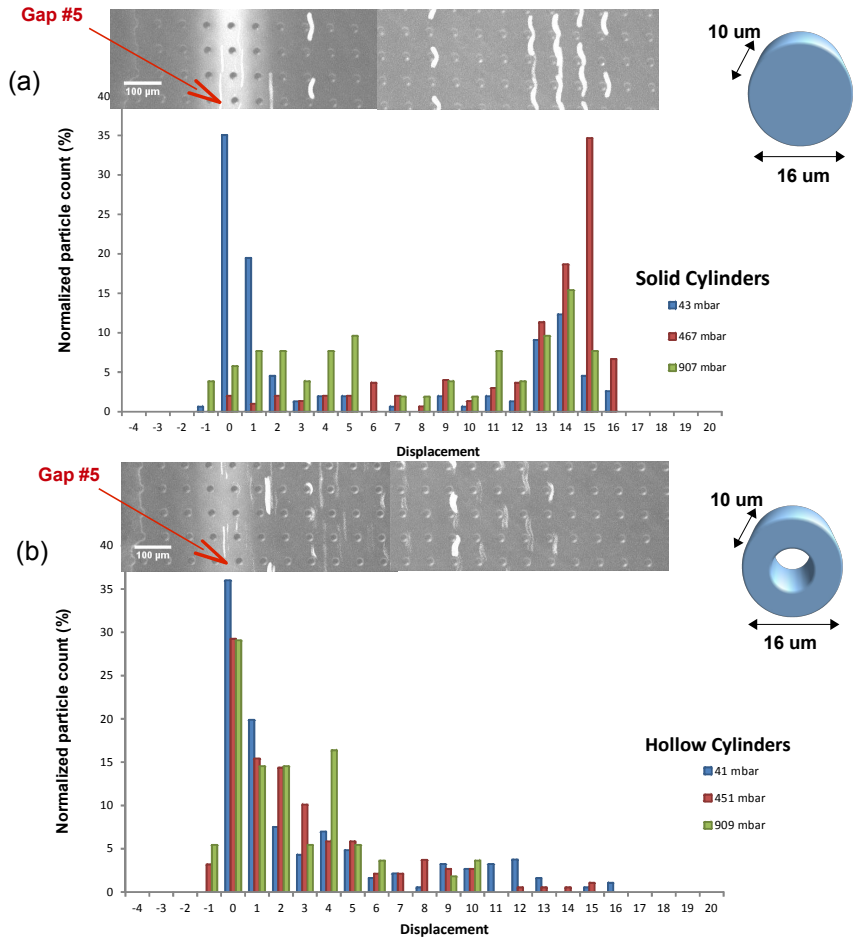

Figure 7.3: The lateral displacement of (a) solid cylinders and (b) hollow cylinders (illustrated schematically on the upper right corner of each graph) in the straight DLD device. The gap #5 corresponds to zero displacement. The fluorescent images above each graph are the result of 1000 frames of position 1 and 2 overlaying on top of each other at 43 *mbar* and 41 *mbar* for solid and hollow cylinders, respectively.

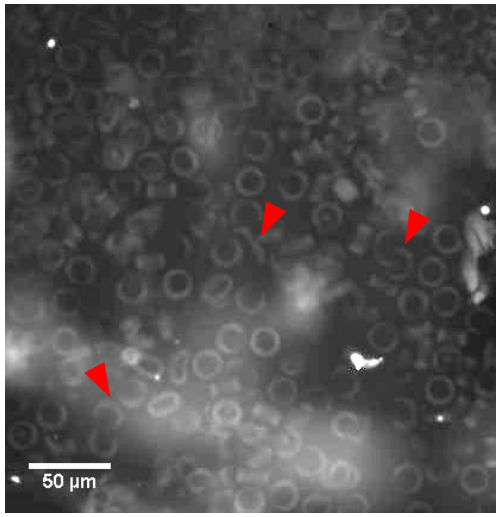

Figure 7.4: 16 μm hollow cylinders in the inlet reservoir of the DLD device. Red arrows point towards the broken particles in the sample. These particles are suspected to show smaller effective size than the unbroken ones.

was plotted against the lateral displacement. As previously discussed (section 6.2), zero displacement corresponds to the nominal gap number 5.

Despite having the same outer dimensions, the fluorescent image analysis and the displacement plots revealed different behaviour of these two types of particles. Regarding solid cylinders, two peaks in outlet distribution were observed. They showed a constant peak in lateral displacement of 15 gaps for all applied pressures. The first peak near zero displacement is most likely due to small debris (half polymerized particles or broken particles as a result of centrifugal force when the particles were collected) present in the sample. The smaller number of counts around zero displacement at higher pressures is because these small particles were more difficult to distinguish from the fluorescent background at those pressures.

In the case of hollow cylinders, apart from the peak around zero displacement, no noticeable peak was observed. Instead, they indicated a

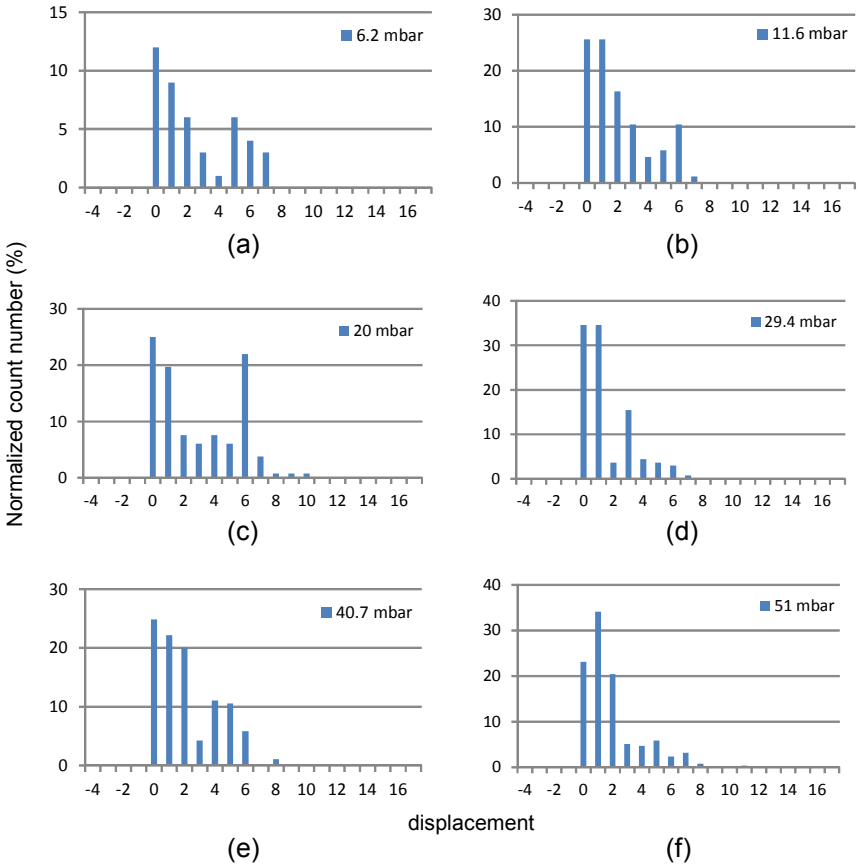

Figure 7.5: The lateral displacement of hollow circle-shaped cylinders at low pressure regime in the DLD device. Zero displacement corresponds to nominal gap number 5. The shear rate increases from 69 s^{-1} to 2.3×10^2 s^{-1} corresponding to the velocities of 8.6×10^{-1} ms^{-1} to 2.9 ms^{-1} for this pressure range.

dispersed outlet distribution. One reason for this non-uniformity in distribution of these particles is that there were some broken particles in the sample (Fig. 7.4). This might be due to insufficient thickness of the particle wall. We assume that provided that the difference between inner and outer diameters is increased, this problem would be diminished.

Since hollow cylinders showed a high degree of deformability even at the lowest applied pressure of this set of experiments (41 $mbar$), we decided to run the same experiment in the low pressure regime. The pressure was increased from 6.2 to 51 $mbar$ corresponding to shear rates of 69 s^{-1} to 2.3×10^2 s^{-1}. The results are plotted in figure 7.5. As in the case of high pressures, the particles showed a constant peak around zero displacement. However, the distribution seems to be less dispersed with the largest displacement of 10 gaps.

Chapter 8

Discussion

Comparing the lateral displacement of solid and hollow particles (figures 7.3 and 7.5), the latter shows larger deformability and hence smaller effective size as predicted. The solid cylinders behaved as rigid particles even at the highest applied pressure of 909 $mbar$, whereas hollow cylinders showed a high degree of deformation at the lowest applied pressure of about 6 $mbar$. Thus we can conclude that the deformability ratio for these two types of particle seams to be larger than $\frac{909}{6} \sim 151$.

The behaviour of both these particles needs to be further investigated because even for the same kind of particle, they show different degrees of deformation as shown in figure 8.1. The particles in this figure are 16 μm hollow cylinders at the pressure of 6.2 $mbar$ (the shear rate of 69 s^{-1}). At the same shear rate, different effective sizes are assumed for these particles. The images are ordered according to increase in the effective size ($R_{eff,a} < R_{eff,b} < R_{eff,c} < R_{eff,d}$). The particle in figure 8.1-a, is a broken cylinder which demonstrates the smallest effective size and moves in zig-zag mode when it encounters the first post to the left. Other three particles (Fig. 8.1-b,c,d) are moving in displacement mode. This figure explains the dispersed distribution of the particles at the end of the device.

Prior to discussing the suggestions for the design of future experiments, we will deal with the results of two studies on the behaviour of soft particles.

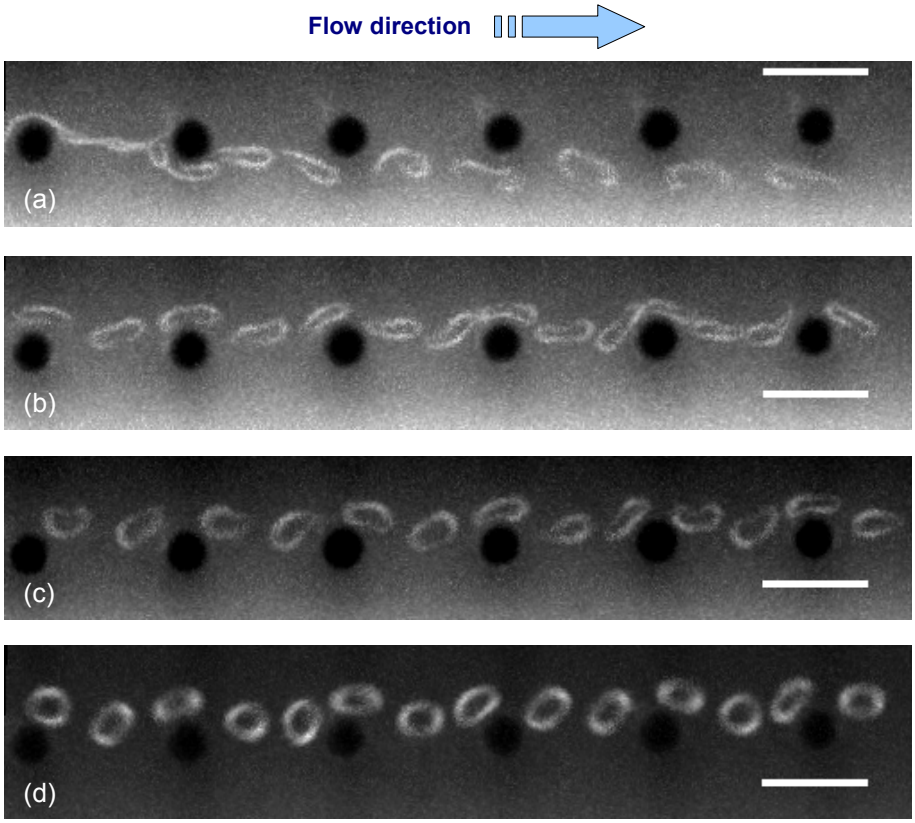

Figure 8.1: Deformation of 16 μm hollow cylinders at the pressure of 6.2 $mbar$. The recordings were done in fluorescence mode with the frame rate of 30 frames per second. The first particle in (a) is a broken cylinder and shows the smallest critical size. The effective size of complete particles increases from (b) to (d). Scale bars are 50 μm.

In the first study by Haghgooie *et al.* [35], they investigated the deformation of four types of disk-, ring-, cross- and star-shaped particles with the diameter of 8 μm and the thickness of 2 μm (but decreasing in volume) in narrow 4 $\mu m \times 4$ μm constriction (Fig. 8.2) [1]. They flowed the the particles into the constrictions at known pressure differences and found the critical threshold pressure differential. This pressure was defined as the pressure at which 50% of particles have passed through the constrictions.

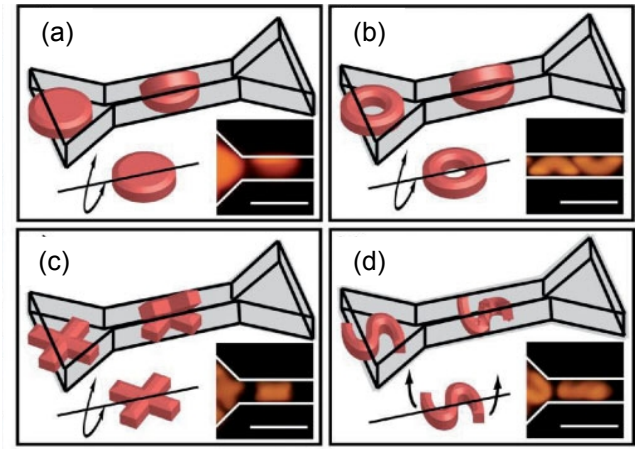

Figure 8.2: The behaviour of (a) disk, (b) ring, (c) cross and (d) S-particles with the dimensions of 8 $\mu m \times 8$ $\mu m \times 2$ μm when they pass through narrow 4 $\mu m \times 4$ μm constrictions. The volume of particles decreases from disks to S-particles. Disks, rings and crosses bend in the constrictions, but S-particles prefer to twist. Scale bars are 10 μm. Figure is reused with permission form Ref. [35].

Between these different-shaped particles, disks and S-particles showed to be the stiffest and the softest, respectively. Except for S-particles which preferred to twist as they deformed, other particles buckled in the constrictions. In contrast to our experiments, these particles did not stretch. But, on the other hand, this study confirms that in addition to the fraction of

[1] As earlier discussed (section 4.2.1), we used the same monomer solution as that they used in this study.

the cross-linking agent in the monomer solution, the degree of deformation and mechanical strength depends on the shape of particles. They also suggested that the distribution of mass might have a role in the mechanical characteristics of the particles.

To make a comparison, the volume of 16 μm solid and hollow cylinders in our case was 8.0×10^3 and 2.3×10^3 μm^3, respectively. The strain energy [2] depends on the volume. Therefore, for the same applied work, less strain (or deformability) is resulted for solid cylinders.

While the large deformability ratio of these two particle types still remains a question, the second study might solve part of the confusion. Gao *et al.* in a very recent analytical study [61] investigated the shape dynamic of non-spherical soft particles in a shear flow. They defined a dimensionless number G as the ratio of viscous forces in the fluid to the elastic forces in the particle. For $G \ll 1$, the elastic forces in the particle dominate the hydrodynamic viscous forces in the fluid. Thus, a particle inclines to preserve its initial shape. For $G > 0$, there are three modes of motion depending on the aspect ratio of the particles.

For instance, considering a cylinder with an elliptical cross-section. For a fixed G, if the aspect ratio (ω_0) is 1 or for a particle with a circular cross-section, it reaches a steady state with a fixed orientation after being rotated and elongated in the shear flow. Even for large deformations, these particles reach a stable configuration. However, at the same time, the elements inside the particle undergo a tank-treading motion.

A slightly elongated particle moves in an oscillatory fashion named as "trembling (TR)" without making a 2π rotation (Fig. 8.3-a). The line in the figure indicates the long axis of the particle (along with the longer dimension of the particle with as aspect ratio of less than 1). The third mode of motion is "tumbling (TU)" which occurs for a particle with smaller aspect ratio (Fig. 8.3-b). In this mode, particles rotate fully.

We cannot find a perfect match between this theoretical study with the behaviour of our particles. Because these assumptions have been made for an unbounded flow, while in our case, the steric interaction of the particle

[2] The required work to strain an elastic material.

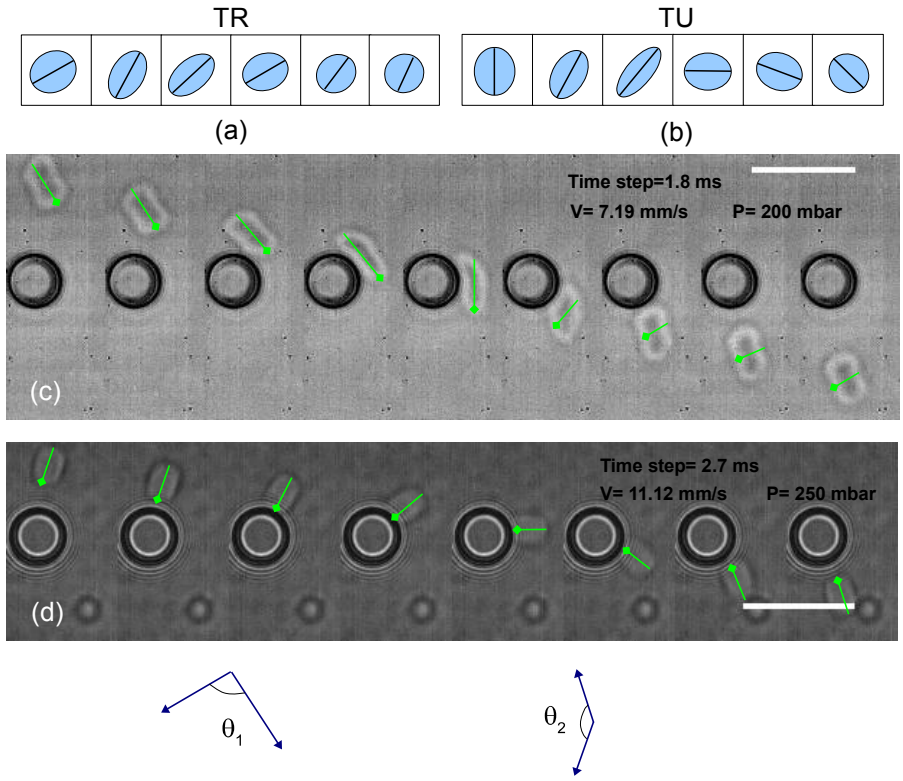

Figure 8.3: 2D simulations based on an analytical study [61] show two modes of motion for soft particles with aspect ratios of less than one in a shear flow: (a) trembling (TR) and (b) tumbling (TU). A particle which is slightly more elongated than a circle (e.g. $\omega_0 = 0.8$) moves in TR mode. It elongates and rotates but not in a full 2π period. A more elongated particle (e.g. $\omega_0 = 0.6$) moves in TU mode making a full 2π rotation. (c) Tracking the axis drawn on the hollow square-shaped cylinder shows this particle makes a $\frac{\pi}{2}$ rotation. It resembles TR mode of motion. θ_1 shows the rotation angle of this particle. (d) The rotation of solid circle-shaped cylinder at the angle of $\theta_2 \sim 180^\circ$ which is analogous to move in both steady sate and TU without elongation. Scale bars are 50 μm.

with the posts should be considered. In spite of the complex behaviour of our particles, some similarities exist. As shown in figure 8.3-c, if we draw an axis along one of the dimensions of the hollow square-shaped particle, we can observe how this axis is elongated and rotates. The rotation angle θ_1 is about 90°. This situation is analogous to TR motion (if we only look at one post) in which the axis becomes elongated and the rotation is not a full 2π rotation. However, after passing four post, the particle rotates fully.

In the case of solid circle-shaped cylinders (Fig. 8.3), the axis rotates considerably ($\theta_2 \sim 180°$) without any noticeable elongation. Remember that this particle rotates from the side face. This mode of motion resembles both the steady state and TU modes. The particle rotates fully after passing two posts but it also keeps its initial shape. While we cannot describe how this behaviour is related to the aspect ratio of these particles, we can suggest different modes of motion for particles with various structures (for instance, hollow and solid structures).

Note that even for rigid ellipsoidal particles which are moving in a uniform shear flow, a preferred direction of motion has been suggested by Jeffrey [62]. According to the "minimum energy" hypothesis, the author showed that at zero Reynolds number, a prolate spheroid prefers to align its polar axis perpendicular to the plane of undisturbed motion of the fluid and rotates about that axis. It resulted in the steady motion of the particle relative to the fluid. In the case of an oblate spheroid, on the other hand, the equatorial axis adjusts itself perpendicular to the plane of undisturbed motion of the fluid. Thus, the particle rotates about its long axis, but the motion is not steady. The periodic rotation takes place with a variable angular velocity.

Turning to our question regarding the large deformability ratio, it can be suggested that solid-structured particles tend to keep their initial shape, while they rotate upon encountering a post. But, hollow-structured particles deform considerably. They also rotate but the angle of rotation decreases with the shear rate (compare the rectangular-shaped cylinder in figure 7.1 with the square-shaped cylinder in figure 8.3).

Moreover, the influence of the aspect ratio for solid particles should be further investigated in future experiments. One more suggestion is to

observe the behaviour of the particles in a simple channel without any posts. To track the particles in the channel, fluorescent microspheres can be added to the particles during polymerization. We tried to polymerize such particles (see figure 4.4-c) , but since adding the beads increased the viscosity of the monomer solution during the polymerization, we stopped synthesizing these particles. However, in future when more time is available, we should try different concentration of the beads to prevent the change in the viscosity to be able to make particles containing beads. This enables us to easily track particles in a channel or in the DLD device.

8.1 Future Directions

Since the aim of this project was to create cell-mimics, some considerations should be regarded in the design of polymeric particles. First, the shape of biological cells as well as their mechanical properties have a major effect in their functionality. The role of particle shape is also important in drug delivery researches. Therefore, to achieve a specific biological response, particles should be designed as the shape of the biological cell of interest [63]. Note that even with a precise design of particles, they would not behave in the same manner as cells, because biological cells respond dynamically to changes in their environment, while synthesized particles cannot [64]. On the other hand, precise control of polymerization conditions including exposure time, temperature, light intensity etc. is necessary.

Moreover, the rotation of the polymeric particles in a simple microfluidic channel would be valuable to examine. Particles containing fluorescence beads can be polymerized. The beads help to track the particles in the channel. Thus, a more exact comparison between our experimental results and the theoretical predictions [61] can be made.

Regarding the DLD device, one suggestion is to design a new DLD device with less difference in critical sizes of successive arrays. In the present device, the critical size was increased in $1 - 1.5\ \mu m$ intervals to span the range of D_c of $10 - 21\ \mu m$. Instead, a device can be designed with a limited range of D_c near to the size of the particles. For instance, providing the

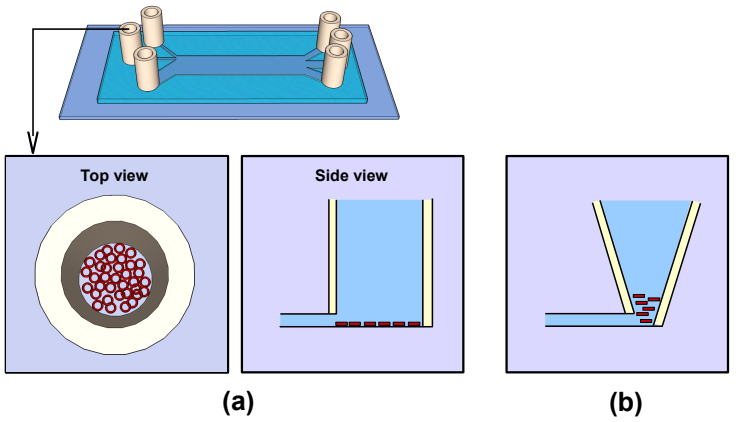

Figure 8.4: (a) The top and the side schematic view of the inlet reservoir containing particles. Particles reside at the bottom of the reservoir due to their higher density than the buffer. (b) If instead of silicon tubes, a pipette tip is used, more particles would move with the flow rather than settling down in the reservoir.

particle of interest is 16 μm in diameter and 10 μm in height, the range of D_c of less than 10 μm (the smallest dimension of the particle) to 16 μm (the largest dimension of the particle) with an increment of 0.5 μm in successive arrays is suggested.

One more idea is that the depth of the DLD device can be changed to see how these particles would behave in that case. As previously mentioned, in devices varying in depth, particles are sorted by their smallest dimensions. Thus, the deformability rate in different dimensions of a particle can be measured.

Last but not least is to find a way to ease the movement of the particles from the inlet reservoir. During these experiments, the buffer was PBS containing 1% v/v Tween 20 with a lower density than that of the hydrogels. Therefore, the denser hydrogel particles settled down in the reservoir resulting in a highly diluted sample stream. This situation is illustrated in figure 8.4-a. Particles are scattered at the bottom of the reservoir. The inlet reservoir can be modified as shown in figure 8.4-b. It is possible to use

a pipette tip instead of the silicon tube which has a narrower exit. Thus, fewer number of particles would be settled down in the reservoir resulting in a higher concentration of particles in the carrying fluid entering the array. Another solution is to use a higher concentrated sample solution to compensate for those which sediment in the reservoir.

Chapter 9

Conclusions

The purpose of this project was to analyse the behaviour of hydrogel particles especially their mechanical properties in the DLD device. Since we can easily control the characteristic parameters of the polymerized particles including the shape, the size and the elasticity, they constitute perfect model cells.

We synthesized polymeric particles in different shapes and sizes in the range of $7-16\ \mu m$. We determined how to recover and store these particles to be used later in DLD devices.

Later, a dedicated DLD device was designed and fabricated to be tested with the polymeric particles. Experiments were performed to observe the deformability rate of the polymeric particles near the posts as a response to increasing shear stress. Moreover, the lateral displacement of two types of particles with the same dimensions but one with hollow structure and the one without any hole was compared.

Both of these investigations revealed the fact that hollow and solid particles behave differently. Solid cylinders seemed to maintain their rigidity even at the highest shear stress, while the hollow ones showed a smaller effective size but a non-uniform lateral displacement. Also, we observed that when the applied pressure is not sufficient to deform the hydrogels, they rotate largely as a result of interaction with the posts.

In conclusion, this was the first step towards constituting a model system for the deformability-based particle sorting in the DLD after the successful separation of RBCs in this device based on their mechanical properties [3]. This research raises new questions and as previously discussed suggests optimization of the DLD device to be able to obtain a detailed analysis of this behaviour.

Bibliography

[1] Lotien Richard Huang, Edward C Cox, Robert H Austin, and James C Sturm. Continuous Particle Separation Through Deterministic Lateral Displacement. *Science*, 304(5673):987–90, 2004.

[2] Dhananjay Dendukuri, Shelley S Gu, Daniel C Pregibon, T Alan Hatton, and Patrick S Doyle. Stop-flow lithography in a microfluidic device. *Lab on a Chip*, 7(7):818–828, 2007.

[3] Jason P Beech, Stefan H Holm, Karl Adolfsson, and Jonas O Tegenfeldt. Sorting cells by size, shape and deformability. *Lab on a Chip*, 12(6):1048–51, 2012.

[4] Stefan H Holm, Jason P Beech, Michael P Barrett, and Jonas O Tegenfeldt. Separation of parasites from human blood using deterministic lateral displacement. *Lab on a Chip*, 11(7):1326–1332, 2011.

[5] Jason P Beech, Peter Jönsson, and Jonas O Tegenfeldt. Tipping the balance of deterministic lateral displacement devices using dielectrophoresis. *Lab on a Chip*, 9(18):2698–2706, 2009.

[6] David J Beebe, Glennys A Mensing, and Glenn M Walker. Physics and applications of microfluidics in biology. *Annual Review of Biomedical Engineering*, 4(1):261–286, 2002.

[7] Bernhard H Weigl, Ron L Bardell, and Catherine R Cabrera. Lab-on-a-chip for drug development. *Advanced Drug Delivery Reviews*, 55(3):349–377, 2003.

[8] Todd M Squires and Stephen R Quake. Microfluidics: Fluid physics at the nanoliter scale. *Reviews of Modern Physics*, 77(July), 2005.

[9] Henrik Bruus. *Theoretical Microfluidics*. Oxford Univ. Press, 2008.

[10] James P Brody and Paul Yager. Diffusion-based extraction in a microfabricated device. *Sensors and Actuators A: Physical*, 58(1):13–18, 1997.

[11] Anne-Laurence Dupont and Gérard Mortha. Comparative evaluation of size-exclusion chromatography and viscometry for the characterisation of cellulose. *Journal of Chromatography A*, 1026(1-2):129–141, 2004.

[12] Marko T Blom, Emil Chmela, R Edwin Oosterbroek, Rob Tijssen, and Albert Van Den Berg. On-chip hydrodynamic chromatography separation and detection of nanoparticles and biomolecules. *Analytical Chemistry*, 75(24):6761–6768, 2003.

[13] John A Davis, David W Inglis, Keith J Morton, David A Lawrence, Lotien R Huang, Stephen Y Chou, James C Sturm, and Robert H Austin. Deterministic hydrodynamics: Taking blood apart. *Proceedings of the National Academy of Sciences of the United States of America*, 103(40):14779–14784, 2006.

[14] David W Inglis, John A Davis, Thomas J Zieziulewicz, David A Lawrence, Robert H Austin, and James C Sturm. Determining blood cell size using microfluidic hydrodynamics. *Journal of Immunological Methods*, 329(1-2):151–156, 2008.

[15] David W Inglis, Keith J Morton, John A Davis, Thomas J Zieziulewicz, David A Lawrence, Robert H Austin, and James C Sturm. Microfluidic device for label-free measurement of platelet activation. *Lab on a Chip*, 8(6):925–931, 2008.

[16] T Kulrattanarak, R G M Van Der Sman, C G P H Schroën, and R M Boom. Classification and evaluation of microfluidic devices for continuous suspension fractionation. *Advances in Colloid and Interface Science*, 142(1-2):53–66, 2008.

[17] Haakan N Joensson, Mathias Uhlén, and Helene Andersson Svahn. Droplet size based separation by deterministic lateral displacement-separating droplets by cell–induced shrinking. *Lab on a Chip*, 11(7):1305–1310, 2011.

[18] Jason P Beech and Jonas O Tegenfeldt. Tuneable separation in elastomeric microfluidics devices. *Lab on a Chip*, 8(5):657–659, 2008.

[19] David W Inglis, Megan Lord, and Robert E Nordon. Scaling deterministic lateral displacement arrays for high throughput and dilution-free enrichment of leukocytes. *Journal of Micromechanics and Microengineering*, 21(5):054024, 2011.

[20] Kevin Loutherback, Kevin S Chou, Jonathan Newman, Jason Puchalla, Robert H Austin, and James C Sturm. Improved performance of deterministic lateral displacement arrays with triangular posts. *Microfluidics and Nanofluidics*, 9(6):1143–1149, 2010.

[21] Keith J Morton, Kevin Loutherback, David W Inglis, Ophelia K Tsui, James C Sturm, Stephen Y Chou, and Robert H Austin. Hydrodynamic metamaterials: microfabricated arrays to steer, refract, and focus streams of biomaterials. *Proceedings of the National Academy of Sciences of the United States of America*, 105(21):7434–7438, 2008.

[22] David W Inglis, John A Davis, Robert H Austin, and James C Sturm. Critical particle size for fractionation by deterministic lateral displacement. *Lab on a Chip*, 6(5):655–658, 2006.

[23] Jason P Beech. *Microfluidics separation and analysis of biological particles*. PhD thesis, Lund University, 2011.

[24] John A Davis. *Microfluidic Separation of Blood Components through Deterministic Lateral Displacement*. PhD thesis, Princeton University, 2008.

[25] Brian R Long, Martin Heller, Jason P Beech, Heiner Linke, Henrik Bruus, and Jonas O Tegenfeldt. Multidirectional sorting modes in deterministic lateral displacement devices. *Physical Review E - Statistical, Nonlinear and Soft Matter Physics*, 78(4 Pt 2):046304, 2008.

[26] Raymond Quek, Duc Vinh Le, and K-H Chiam. Separation of deformable particles in deterministic lateral displacement devices. *Physical Review E - Statistical, Nonlinear and Soft Matter Physics*, 83(5 Pt 2):056301, 2011.

[27] T Kulrattanarak, R G M Van Der Sman, C G P H Schroen, and R M Boom. Analysis of mixed motion in deterministic ratchets via experiment and particle simulation. *Microfluidics and Nanofluidics*, 10(4):843–853, 2011.

[28] Joelle Frechette and German Drazer. Directional locking and deterministic separation in periodic arrays. *Journal of Fluid Mechanics*, 627(2009):379, 2009.

[29] Manuel Balvin, Eunkyung Sohn, Tara Iracki, German Drazer, and Joelle Frechette. Directional locking and the role of irreversible interactions in deterministic hydrodynamics separations in microfluidic devices. *Physical Review Letters*, 103(7):078301, 2009.

[30] Kevin Loutherback, Jason Puchalla, Robert Austin, and James Sturm. Deterministic Microfluidic Ratchet. *Physical Review Letters*, 102(4):1–4, 2009.

[31] David W Inglis. Efficient microfluidic particle separation arrays. *Applied Physics Letters*, 94(1):013510, 2009.

[32] Younan Xia and George M Whitesides. Soft Lithography. *Annual Review of Materials Science*, 28(1):153–184, 1998.

[33] Y Lu, Y Yin, and Y Xia. Three-Dimensional Photonic Crystals with Non-spherical Colloids as Building Blocks. *Advanced Materials*, 13(6):415–420, 2001.

[34] Robert Langer and David A Tirrell. Designing materials for biology and medicine. *Nature*, 428(6982):487–492, 2004.

[35] Ramin Haghgooie, Mehmet Toner, and Patrick S Doyle. Squishy nonspherical hydrogel microparticles. *Macromolecular Rapid Communications*, 31(2):128–134, 2010.

[36] K S Anseth and J A Burdick. New directions in photopolymerizable biomaterials. *MRS Bulletin*, 27(2):130–136, 2002.

[37] Dhananjay Dendukuri and Patrick S Doyle. The Synthesis and Assembly of Polymeric Microparticles Using Microfluidics. *Advanced Materials*, 21(41):4071–4086, 2009.

[38] Dhananjay Dendukuri, Daniel C Pregibon, Jesse Collins, T Alan Hatton, and Patrick S Doyle. Continuous-flow lithography for high-throughput microparticle synthesis. *Nature Materials*, 5(5):365–9, 2006.

[39] Ki Wan Bong, Daniel C Pregibon, and Patrick S Doyle. Lock release lithography for 3D and composite microparticles. *Lab on a Chip*, 9(7):863–866, 2009.

[40] Ji-Hyun Jang, Dhananjay Dendukuri, T Alan Hatton, Edwin L Thomas, and Patrick S Doyle. A route to three-dimensional structures in a microfluidic device: stop-flow interference lithography. *Angewandte Chemie International Edition*, 46(47):9027–31, 2007.

[41] Ki Wan Bong, Ki Tae Bong, Daniel C Pregibon, and Patrick S Doyle. Hydrodynamic focusing lithography. *Angewandte Chemie International Edition*, 49(1):87–90, 2010.

[42] Daniel C Pregibon, Mehmet Toner, and Patrick S Doyle. Multifunctional encoded particles for high-throughput biomolecule analysis. *Science*, 315(5817):1393–1396, 2007.

[43] Priyadarshi Panda, Kai P Yuet, T Alan Hatton, and Patrick S Doyle. Tuning curvature in flow lithography: a new class of concave/convex particles. *Langmuir The Acs Journal Of Surfaces And Colloids*, 25(10):5986–5992, 2009.

[44] Dae Kun Hwang, John Oakey, Mehmet Toner, Jeffrey A Arthur, Kristi S Anseth, Sunyoung Lee, Adam Zeiger, Krystyn J Van Vliet, and Patrick S Doyle. Stop-flow lithography for the production of shape-evolving degradable microgel particles. *Journal of the American Chemical Society*, 131(12):4499–4504, 2009.

[45] Priyadarshi Panda, Shamsher Ali, Edward Lo, Bong Geun Chung, T Alan Hatton, Ali Khademhosseini, and Patrick S Doyle. Stop-flow lithography to generate cell-laden microgel particles. *Lab on a Chip*, 8(7):1056, 2008.

[46] Dhananjay Dendukuri, Priyadarshi Panda, Ramin Haghgooie, Ju Min Kim, T Alan Hatton, and Patrick S Doyle. Modeling of Oxygen-Inhibited Free Radical Photopolymerization in a PDMS Microfluidic Device. *Macromolecules*, 41(22):8547–8556, 2008.

[47] Christian Decker and Aubrey D Jenkins. Kinetic approach of oxygen inhibition in ultraviolet- and laser-induced polymerizations. *Macromolecules*, 18(6):1241–1244, 1985.

[48] Subra Suresh. Biomechanics and biophysics of cancer cells. *Acta Biomaterialia*, 3(4):413–438, 2007.

[49] R M Hochmuth. Micropipette aspiration of living cells. *Journal of Biomechanics*, 33(1):15–22, 2000.

[50] R E Mahaffy, C K Shih, F C MacKintosh, and J Käs. Scanning probe-based frequency-dependent microrheology of polymer gels and biological cells. *Physical Review Letters*, 85(4):880–883, 2000.

[51] Quan Guo, Sunyoung Park, and Hongshen Ma. Microfluidic Micropipette Aspiration for Measuring the Deformability of Single Cells. *Lab Chip*, 2012.

[52] Bryan Lincoln, Harold M Erickson, Stefan Schinkinger, Falk Wottawah, Daniel Mitchell, Sydney Ulvick, Curt Bilby, and Jochen Guck.

Deformability-based flow cytometry. *Cytometry Part A the journal of the International Society for Analytical Cytology*, 59(2):203–209, 2004.

[53] Jochen Guck, Stefan Schinkinger, Bryan Lincoln, Falk Wottawah, Susanne Ebert, Maren Romeyke, Dominik Lenz, Harold M Erickson, Revathi Ananthakrishnan, Daniel Mitchell, Josef Käs, Sydney Ulvick, and Curt Bilby. Optical deformability as an inherent cell marker for testing malignant transformation and metastatic competence. *Biophysical Journal*, 88(5):3689–3698, 2005.

[54] Hansen Bow, Igor V Pivkin, Monica Diez-Silva, Stephen J Goldfless, Ming Dao, Jacquin C Niles, Subra Suresh, and Jongyoon Han. A microfabricated deformability-based flow cytometer with application to malaria. *Lab on a Chip*, 11(6):1065–1073, 2011.

[55] H W Hou, A A S Bhagat, P Mao, J Han, and C T Lim. Deformability based cell margination for malaria infected red blood cell enrichment . *World Health*, (October):1370–1372, 2010.

[56] Soojung Claire Hur, Nicole K Henderson-MacLennan, Edward R B McCabe, and Dino Di Carlo. Deformability-based cell classification and enrichment using inertial microfluidics. *Lab on a Chip*, 11(5):912–920, 2011.

[57] Quan Guo, Sarah M McFaul, and Hongshen Ma. Deterministic microfluidic ratchet based on the deformation of individual cells. *Physical Review E*, 83(5, Part 1), 2011.

[58] Sarah M. McFaul, Bill K. Lin, and Hongshen Ma. Cell separation based on size and deformability using microfluidic funnel ratchets. *Lab Chip*, 2012.

[59] John P Arata and Alexander Alexeev. Designing microfluidic channel that separates elastic particles upon stiffness. *Soft Matter*, 5(14):2721, 2009.

[60] O Berk Usta, Michael Nayhouse, Alexander Alexeev, and Anna C Balazs. Designing patterned substrates to regulate the movement of capsules in microchannels. *The Journal of chemical physics*, 128(23):235102, 2008.

[61] Tong Gao, Howard H. Hu, and Pedro Ponte Castañeda. Shape dynamics and rheology of soft elastic particles in a shear flow. *Phys. Rev. Lett.*, 108:058302, Jan 2012.

[62] G B Jeffery. The Motion of ellipsoidal particles immersed in viscous fluid. *Proceedings of the Royal Society A Mathematical Physical and Engineering Sciences*, 102:161–179, 1922.

[63] Samir Mitragotri and Joerg Lahann. Physical approaches to biomaterial design. *Nature Materials*, 8(1):15–23, 2009.

[64] G Bao and S Suresh. Cell and molecular mechanics of biological materials. *Nature Materials*, 2(11):715–725, 2003.

Appendix A:
Master Fabrication

The silicon master was fabricated using UV lithography. The involved procedures are described here:

1. A clean $4''$ wafer was baked at $200°C$ for 4 hours.

2. After 1 min relaxation, the wafer was spin-coated with the photoresist SU8 2050 (10 s spinning at 500 rpm at the slowest acceleration followed by 60 s spinning at 3200 rpm at the highest acceleration.

3. The resist residual was removed from the edge of the wafer by dipping in developer.

4. In the next step, the wafer was soft-baked for 3 min at $65°C$ followed by 10 min at $95°C$.

5. After 5 min relaxation, the wafer was mounted in a mask aligner and exposed to UV light (20 mW/cm^2 with l-line filter) in vacuum contact mode for 7 s.

6. Next, 4 min relaxation was followed by post exposure baking (PEB) as in step 4.

7. The wafer was developed in SU8 developer in an ultrasonic bath for 5 min at 110 V.

8. The wafer was hard-baked for 30 min at $200°C$.

9. Finally, the surface of the master is treated with the anti-sticking agent (1H,1H,2H,2H-perfluorooctyltrichlorosilnae).

Appendix B:
PDMS Microfabrication

In this chapter, the fabrication of a PDMS device using a patterned silicon master is explained:

1. PDMS is mixed with the curing agent at the ratio of 10:1 and degassed in the vacuum for 30 min.

2. Then, the degassed PDMS is poured on the master and cured at $80°C$ for one hour.

3. The PMDS slab is pealed off from the master and the holes punched on top of the reservoir pads.

4. The PDMS slab and the glass substrate are bonded together using oxygen plasma.

5. The reservoir tubes are glued on top of the holes with silicon adhesive (A07, Wacker Silicones). The device is let to be dries for 1-2 hour.

6. In the case of the microfluidic channel for particle polymerization, the reservoirs are filled with 2% v/v Tween20 in PBS over night.

7. In the case of DLD device, the device was treated with the anti-sticking in glove box at $180°C$ for about 8 hours.

Appendix C:
Particle Polymerization

The monomer solution for the synthesis of hydrogels consists of:

DI water	20% v/v
UV-initiator	15% v/v
PEG solution	65% v/v

The PEG solution contains PEG diacrylate with a molecular weight of 700 and PEG with a molecular weight of 200. The fraction of PEG 700 determines the deformability of the hydrogels. We used the 20% of the PEG 700 in the PEG solution which corresponds to 13% of the whole solution. The particles become stiffer with an increase in the PEG 700 fraction.

To make fluorescent particles 1% of rhodamibe B was added to the solution.

Lund University